

Rapid Versus Delayed Linkage and Coalescence of Propagating Rift Tips

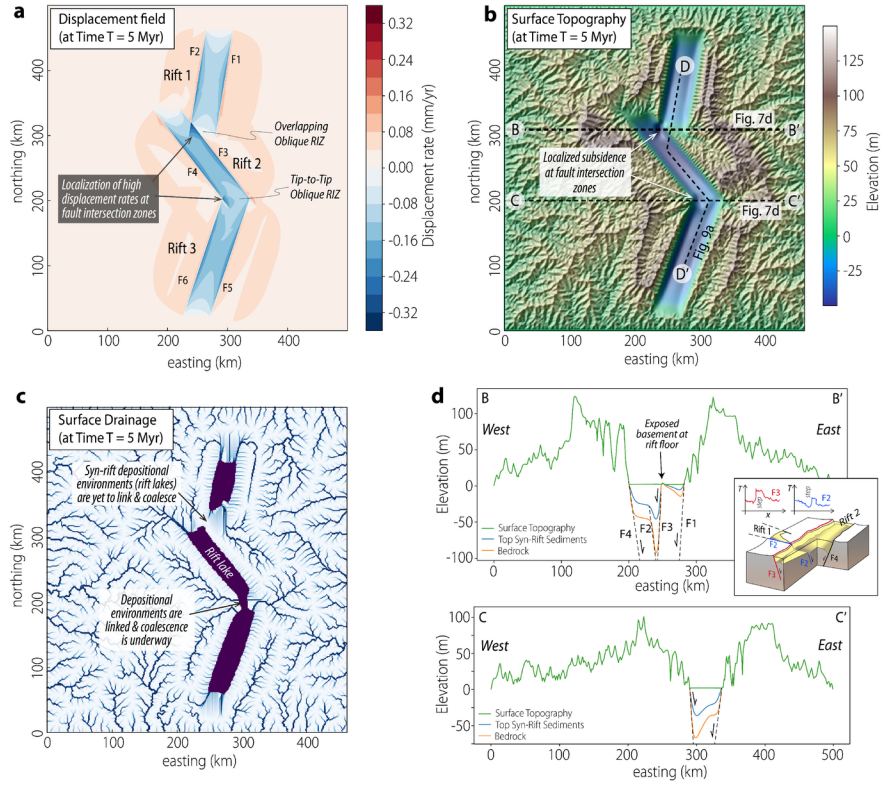
Folarin Kolawole¹, Liang Xue¹, and Zuze Dulanya¹

¹Affiliation not available

March 04, 2024

Abstract

The tectonic interaction, linkage, and coalescence of propagating continental rift segments eventually create a through-going axial rift floor without which a break-up axis cannot develop. However, prior to linkage, interacting rifts are separated by a topographic basement-high (rift interaction zone, RIZ) which is progressively dismembered and down-thrown by the lateral propagation of rift-tip faulting and their hanging wall subsidence. Here, we explore the evolution of the Middle Shire and Nsanje RIZs located along three contiguous non-volcanic propagating rift segments: the southern Malawi Rift (SMR), Lower Shire Graben (LSG), and the Nsanje Graben (NG), East Africa. The Middle Shire RIZ is an overlapping-oblique divergent RIZ in which the NNE/N-trending SMR is propagating southwards into the shoulder of the NW-trending LSG, whereas the Nsanje RIZ is a tip-to-tip oblique RIZ in which the LSG has propagated southeast into the northern tip of the N-trending NG. We utilize field observations and a landscape evolution model with implemented fault displacement fields of two contiguous RIZs with contrasting geometries, to simulate their geomorphic evolution, and apply a static stress model to evaluate the stress transfer patterns during RIZ evolution. The model results provide insights into the natural observations in the study area, in which, with progressive extension and tip growth, the Middle Shire RIZ maintains minor basement down-throw and an unequilibrated axial stream profile, which contrasts the widespread basement burial and equilibrated axial stream profile across the Nsanje RIZ. Modeled static stress distribution predicts compounding stress concentrations at tip-to-tip RIZs (synthetic border fault interactions), favoring brittle strain localization and rift coalescence, and stress relaxation at overlapping divergent RIZs (antithetic border fault interactions), favoring stalled rift coalescence. We argue that RIZ and rift border fault geometries, and their kinematics strongly influence the pace of rift coalescence by modulating the spatial distribution of tectonic stresses necessary to promote rift-linking deformation.



1 This manuscript has been peer-reviewed and accepted for publication in **AGU Books: Extensional**
2 **Tectonics: Continental Breakup to Formation of Oceanic Basins**. Shortly, the “Peer-reviewed
3 publication DOI” link will be updated on this preprint server. We hope you find this paper interesting
4 and would welcome your feedback on it.

5 Kindly contact Folarin Kolawole (folo@ldeo.columbia.edu) with any feedback that you may have.

6

7

Accepted

8 **Rapid Versus Delayed Linkage and Coalescence of Propagating Rift Tips**

9 Folarin Kolawole^{1*}, Liang Xue², Zuze Dulanya³

10 ¹Department of Earth and Environmental Sciences, Lamont-Doherty Earth Observatory of Columbia
11 University, New York, USA

12 ²Department of Earth and Environmental Sciences, Syracuse University, Syracuse, NY, USA

13 ³Geography and Earth Sciences Department, University of Malawi, Zomba, Malawi

14 Correspondence to: F. Kolawole (fola@ldeo.columbia.edu)

15

16 **Abstract**

17 The tectonic interaction, linkage, and coalescence of propagating continental rift segments eventually
18 create a through-going axial rift floor without which a break-up axis cannot develop. However, prior
19 to linkage, interacting rifts are separated by a topographic basement-high (rift interaction zone, RIZ)
20 which is progressively dismembered and down-thrown by the lateral propagation of rift-tip faulting
21 and their hanging wall subsidence. Here, we explore the evolution of the Middle Shire and Nsanje
22 RIZs located along three contiguous non-volcanic propagating rift segments: the southern Malawi Rift
23 (SMR), Lower Shire Graben (LSG), and the Nsanje Graben (NG), East Africa. The Middle Shire RIZ
24 is an overlapping-oblique divergent RIZ in which the NNE/N-trending SMR is propagating
25 southwards into the shoulder of the NW-trending LSG, whereas the Nsanje RIZ is a tip-to-tip oblique
26 RIZ in which the LSG has propagated southeast into the northern tip of the N-trending NG. We
27 utilize field observations and a landscape evolution model with implemented fault displacement fields
28 of two contiguous RIZs with contrasting geometries, to simulate their geomorphic evolution, and
29 apply a static stress model to evaluate the stress transfer patterns during RIZ evolution. The model
30 results provide insights into the natural observations in the study area, in which, with progressive
31 extension and tip growth, the Middle Shire RIZ maintains minor basement down-throw and an
32 unequilibrated axial stream profile, which contrasts the widespread basement burial and equilibrated
33 axial stream profile across the Nsanje RIZ. Modeled static stress distribution predicts compounding
34 stress concentrations at tip-to-tip RIZs (synthetic border fault interactions), favoring brittle strain
35 localization and rift coalescence, and stress relaxation at overlapping divergent RIZs (antithetic border
36 fault interactions), favoring stalled rift coalescence. We argue that RIZ and rift border fault geometries,
37 and their kinematics strongly influence the pace of rift coalescence by modulating the spatial
38 distribution of tectonic stresses necessary to promote rift-linking deformation.

39

40 *Keywords: Continental Rift, Rift Linkage, Rift Interaction Zone, Landscape Evolution*

41

42

43

44

45

46 1. Introduction

47 In continental lithosphere, the initiation of a divergent plate boundary is manifested by the
48 development of a system of isolated graben and half-graben rift basins, each representing a rift
49 segment (Figure 1a; e.g., Rosendahl et al., 1986; Rosendahl 1987; Ebinger et al., 1987; Corti et al.,
50 2007; Nelson et al., 1992; Kolawole et al., 2021a). Some rift segments may nucleate as a system of sub-
51 basins with early establishment of the length of the entire border fault system (Rotevatn et al., 2018),
52 whereas others nucleate by a progressive lateral growth of the border fault (Agar and Klitgord, 1995).
53 In narrow continental rift systems, although nucleating rift border faults may initially terminate at mis-
54 oriented pre-rift basement shear zones or strong crustal blocks, stress build-up and magmatism at rift
55 tips may drive renewed propagation of the rift basin (Ebinger et al., 1989; van Wijk and Blackman,
56 2005; Kolawole et al., 2022). With continued tectonic extension of the lithosphere, which may occur
57 over multiple rift phases, rift basins deepen and lengthen by means of the three-dimensional
58 propagation of their basin-bounding and intrabasinal fault systems, during which tectonic strain may
59 migrate between the faults and sub-basins (e.g., Ebinger et al., 1989, 2000; Heilman et al; 2019;
60 Fazlikhani et al., 2021; Scholz et al., 2020; Kolawole et al., 2022; Shaban et al., 2023). However, the
61 inherited crustal rheology may temporarily stagnate the lateral propagation of a rift tip (e.g., van Wijk
62 and Blackman, 2005; Kolawole et al., 2022; Shaban et al., 2023), during which mantle flow patterns
63 beneath the rift tip promote stress build-up and shear zone formation (e.g., van Wijk and Blackman,
64 2005). As propagating rift tips encroach into un rifted basement areas in the intervening region between
65 the rift segments, their faults may interact and transfer tectonic strain, leading to the hard- and/or
66 soft-linkage of the faults (Figures 1b-c; McClay and Khalil, 1998; McClay et al., 2002; Fossen and
67 Rotevatn, 2016; Kolawole et al., 2021a). These intervening regions of un rifted basement are usually of
68 large spatial scales (~100 – 200-km length scales) and are referred to as Rift Interaction Zones (RIZ
69 in Figures 1a-c; Nelson et al., 1992; Koehn et al., 2008; Aanyu and Koehn, 2011; Sachau et al., 2015;
70 Kolawole et al., 2021a). It is within this broad RIZ region that relatively smaller-scale (~50 km length
71 scale) deformation and strain transfer features such as ‘Transfer Zones’ and ‘Accommodation Zones’
72 develop to facilitate rift linkage (Figures 1a-b; Bosworth, 1985; Ebinger et al., 1987; Coffield and
73 Schamel, 1989; Morley et al., 1990; Morley, 1995; Faults and Varga, 1998; Withjack et al., 2002).

74 Eventually, the linkage of the propagating rift segments is succeeded by the coalescence of the rift
75 basins, forming a composite rift basin with a through-going rift floor of pronounced crustal
76 subsidence and significant basement burial along a localized narrow rift system (Figure 1c). RIZs
77 constitute ‘sticky crustal blocks’, and the significance of rift segment coalescence is founded on the
78 grounds that a successful through-going break-up axis cannot develop along an evolving continental
79 rift system without the structural breaching of its RIZs. During the process of rift linkage, a deforming
80 RIZ transitions from an unbreached RIZ, to partially breached, and breached RIZ; where an additional
81 stage of ‘recently breached’ RIZ is observable in modern active continental rift systems (Kolawole et
82 al., 2021a). Also, the maximum length of a rift border fault is determined by the effective elastic
83 thickness of the lithosphere (Ebinger et al., 1999), such that after the coalescence of isolated rift basins,
84 the resulting composite rift basin is made up of multiple border fault systems that flip polarity along-
85 strike (e.g., Bosworth, 1985; Rosendahl et al., 1986; Ebinger et al., 1987; Rosendahl, 1987; Sander and
86 Rosendahl, 1989; Patton et al., 1994; Lao-Davila et al., 2016; Heilman et al., 2019). Segmentation zones
87 of extensional systems also play important roles during the mature stages of divergent plate boundary
88 development. For example, during continental break-up, delayed propagation of the break-up axis

89 (oceanic ridge tip) promotes excess magmatism at the segmentation zones where the ridge propagation
90 is stalled (Koopmann et al., 2014).

91 Analog and numerical modeling experiments of rift linkage, mostly focused on underlapping and
92 overlapping parallel rift segments, show that various kinematics of faulting may develop in the zone
93 of rift interaction, with geometrical and mechanical controls of inherited basement structure (e.g.,
94 Wilson, 1990; Acocella et al., 1999; Corti, 2004; Aanyu and Koehn, 2011; Corti, 2012; Neuharth et al.,
95 2021; Wolf et al., 2022). Indeed, a few recently published models incorporated obliquely oriented rifts
96 (Molnar et al., 2019; Schmid et al., 2023). However, natural rift systems exhibit a broader variety of
97 three-dimensional RIZ geometries which include tip-to-tip, oblique, and orthogonal plan-view
98 geometries for rift pairs in which the rift border faults, although separated by up to 300 km, may have
99 synthetic dip polarity defining a ‘convergent’ geometry or are antithetic to one another representing a
100 ‘divergent’ geometry (Kolawole et al., 2021a). Although RIZs are larger-scale structures than Transfer
101 Zones, the convention of ‘convergent’ and ‘divergent’ terminology to describe the 3-D structure of
102 RIZs is adopted from the Transfer Zone classification of Morley et al. (1990). The complexity of RIZ
103 geometries also encompasses triple and quadruple junctions that feature three or more juvenile rift
104 segments (Kolawole et al., 2021a). Some of the enigmatic RIZ geometries are the overlapping
105 divergent RIZs in which the rifts are oriented obliquely or orthogonally to one another, such that the
106 border faults of a rift segment are propagating into the uplifting footwall of the border faults (or rift
107 flank) of the other rift basin. The diverse RIZ geometries demonstrate a greater three-dimensional
108 complexity than the simple parallel and overlapping geometries commonly adopted in many published
109 numerical and analog modeling studies of rift segment interaction.

110 In this contribution, we investigate the potential tectonic factors that may promote, inhibit, or delay
111 the pace of rift linkage and coalescence, and test the hypothesis that RIZ geometry and the associated
112 kinematics may constitute one of these factors. We explore the structure, fault kinematics,
113 displacement and stress transfer fields, and landscape evolution of two RIZs separating three
114 contiguous actively propagating magma-poor rift segments in the southern East African Rift System:
115 the southern Malawi Rift, Lower Shire Graben, and the Nsanje Graben (Figure 2). The Middle Shire
116 RIZ is an overlapping oblique divergent RIZ in which the NNE/N-trending southern Malawi Rift is
117 propagating southwards into the NE shoulder of the NW-trending Lower Shire Graben, whereas the
118 Nsanje RIZ is a tip-to-tip oblique RIZ (convergent) in which the Lower Shire Graben has propagated
119 southeast into the northern tip of the N-trending Nsanje Graben. The two RIZs provide natural
120 examples to explore strain localization on rift tips and RIZ syn-rift evolution in the absence of
121 magmatism. We utilize field observations, landscape evolution, and static stress distribution models
122 to examine the potential influence of the contrasting RIZ geometries on the long-term evolution of
123 the RIZs.

124

125 **1.1. The Zomba - Lower Shire - Nsanje Rift Zone**

126 1.1.1. Pre-Rift Basement Geology

127 The east African basement is characterized by Archean and Paleoproterozoic cratonic blocks that are
128 surrounded by Meso- to Neoproterozoic orogenic belts (Fritz et al., 2013). The orogenic belts are
129 composed of exhumed igneous and metamorphic rocks of mostly amphibolite to granulite facies

130 grades, with sporadic occurrences of eclogite facies rocks that are localized along ductile terrane
131 boundary shear zones (e.g., Daly et al., 1991; Fritz et al., 2013). These orogenic belts developed during
132 multiple Meso- to Neoproterozoic orogenic events that witnessed the amalgamation of Gondwana
133 (Fritz et al., 2013). In the Phanerozoic, East Africa has experienced repeated phases of tectonic
134 extension, in which the rift systems follow the mobile belts and avoid the cratonic blocks (Daly et al.,
135 1989; Corti et al., 2007).

136 The southern Malawi Rift and Shire Rift Zone developed along tectonic boundaries that separate
137 distinct Precambrian orogenic belts or terranes. These include the Southern Irumide Belt (1060 - 950
138 Ma), Zambezi Belt (1830 - 795 Ma), the Tete-Chipata Complex, and the Unango Complex (1060 - 950
139 Ma) (Barr and Brown, 1987; Hargrove et al 2003; Fritz et al., 2013) (Figure S1), whereas the Nsanje
140 Graben developed within the Nampula Complex (1025-1075 Ma). The basement terranes along these
141 mobile belts are composed of Mesoproterozoic crust which has been reworked and overprinted by
142 contractional structures and igneous intrusions of the Neoproterozoic Pan African Orogeny.
143 Common rock types found in the mobile belts include schists, amphibolite and granulitic gneisses,
144 deformed granites, granodiorites, syenites, gabbro, and anorthosites (e.g., Barr and Brown, 1987; Fritz
145 et al., 2013).

146

147 1.1.2. Rift Structure and Tectonic History

148 The Phanerozoic Eon of eastern Africa has witnessed three distinct phases of tectonic extension that
149 localized rift basins along the Precambrian mobile belts (Delvaux, 1989; Castaing, 1991; Chorowicz,
150 2005). The first rifting phase occurred in the Permian – Early Jurassic, known as the ‘Karoo’ event,
151 the second event occurred in the Late Jurassic - Cretaceous, and the third event is the current phase
152 of tectonic extension known as the ‘East African Rift System’ (EARS; Delvaux, 1989; Castaing, 1991).
153 The rift system is characterized by a network of rift segments that define multiple branches, mainly
154 the Eastern, Western, Southern, and Southwestern branches (Figure 2). The Eastern Branch is magma-
155 rich manifested by widespread volcanism along the rift basins; whereas the Western, Southern, and
156 Southwestern branches are largely magma-poor with surface volcanism restricted to four rift
157 interaction zones (Figure 2). The Karoo and Cretaceous rift segments and associated faults were
158 commonly reactivated in the Cenozoic rift phase (Castaing, 1991; Morley et al., 1999; Daly et al., 2020;
159 Kolawole et al., 2018; 2021b, 2022). However, there is increasing evidence suggesting that the
160 transition from Mesozoic to Cenozoic rifting phases was accompanied by the abandonment of some
161 of the early-rift fault segments, sub-basins, and in some cases, entire rift segments (e.g., blue lines of
162 ‘inactive rifts’ in Figure 2; Delvaux, 1989; Castaing, 1991; Ragon et al., 2019; Kolawole et al., 2022).
163 Considering the history pronounced magmatic Karoo and Cretaceous rifting in the southern Malawi-
164 central Mozambique region, the ‘pre-rift basement’ of the Cenozoic rift phase is characterized by a
165 basal Precambrian metamorphic unit and its overlying volcano-sedimentary sequences of Mesozoic
166 rift deposits (Castaing, 1991; Kolawole et al., 2021).

167 The Zomba, Lower Shire, and Nsanje grabens define a system of three contiguous active rift basins
168 that extend between the southern Malawi and central Mozambique regions of EARS’s magma-poor
169 southern branch (Figure 2). Thermochronological modeling suggests that the border faults have been
170 active since the Late Oligocene - Early Miocene, with a possible onset of Cenozoic rifting as early as

171 the Eocene (Bicca et al., 2019; Ojo et al., 2022a). Current geodetic extension rates in the region is ca.
172 2.2 mm/yr (Stamps et al., 2018), with a regional normal faulting stress regime of ENE-WSW-oriented
173 minimum principal compressive stress axis, σ_3 (Williams et al., 2019) (Figure 3a). Geodetic extension
174 rates vary along-trend of the Malawi Rift (Saria et al., 2014). Seismic- and gravity-derived estimates of
175 crustal thickness beneath the grabens range ca. 40 - 43 km (Njinju et al., 2019; Sun et al., 2021);
176 lithospheric thickness is ca. 130 km, but thins to ca. 110 km beneath the Shire Rift Zone (Njinju et al.,
177 2019a). The distribution of aeromagnetic Curie Point depths suggests an elevated heat flow of ca. 76
178 mWm^{-2} within the grabens relative to the ca. 66 mWm^{-2} in the rift flanks (Njinju et al., 2019b).

179 The NNE-trending Zomba Graben is the southernmost section of the Malawi Rift and is bounded
180 by the Zomba Fault to the east and Lisungwe and Wamkurumadzi Fault systems to the west (Figure
181 3a). The border faults generally follow the large-scale trends of the Precambrian metamorphic fabrics,
182 indicating basement control on border fault localization (Williams et al., 2019; Kolawole et al., 2021a).
183 Rift sedimentation in the Zomba Graben is primary localized in the northern, northeastern, and
184 western parts of the graben (Figure 3b) and are dominated by unconsolidated Quaternary fluvial
185 deposits and outcrops of clay-rich Matope paleo-lake sediments with characteristic shoreline gravels
186 (Dulanya, 2017). The southern section of the graben is dominated by Precambrian basement
187 exposures along the rift floor (Figure 3b; Kolawole et al., 2021a). The magnitudes of cumulative border
188 fault offset along the Malawi Rift generally decrease southward, and the deepest syn-rift sedimentary
189 sequences in the northern sub-basins of the rift appear to be absent in the south, suggesting an overall
190 long-term southward propagation of the rift basin (Specht and Rosendahl, 1989; Scholz et al., 2020).
191 South of Lake Malawi, shallow boreholes, electrical resistivity tomography, and depth-to-magnetic
192 basement show rift sediment thickness of not more than 600 m (Bloomfield, 1965; Ojo et al., 2022b).

193 The NW-trending Lower Shire Graben is located south of the Zomba Graben and represents the
194 easternmost sub-basin of the Shire Rift Zone, a multiphase rift basin in east Africa (Castaing, 1991;
195 Kolawole et al., 2022). The Lower Shire Graben is bounded to the northeast by the Thyolo-Muona-
196 Ruo Fault System in the east and to the southwest by the Panga Fault. The basin shows widespread
197 coverage of Quaternary deposits (Figure 3b), with the thickest sections potentially occurring in the
198 hanging wall of the Thyolo and Muona faults, dominated by the fluviolacustrine sequences of the
199 Elephant Marsh and Shire River (Kolawole, 2020; Kolawole et al., 2022). The localization of the
200 Elephant Marsh along the hanging wall of the Thyolo Fault, and the spatial correlation of the lateral
201 changes in the geometry of the marsh with prominent changes in the Thyolo Fault displacement
202 profile suggest structural control on the development of the wetland (Kolawole, 2020). The rift axis
203 hosts a buried segment of a large-offset fault, the southern segment of the Mwanza Fault, which is
204 interpreted to be the eastern border fault of the Shire Rift Zone during the Mesozoic phases of
205 extension (Kolawole et al., 2022). Similar to the Zomba Graben, the Mwanza and the Thyolo-Muona-
206 Ruo border fault systems of the Lower Shire Graben generally follow the large-scale trends of the
207 Precambrian metamorphic fabrics, indicating basement control on border fault localization (Wedmore
208 et al., 2020a; Kolawole et al., 2022). However, the southeastern tip of the Ruo Fault crosscuts the NE-
209 trending basement fabrics of the Precambrian Lurio Shear Zone (Kolawole et al., 2022). Outcrops of
210 Mesozoic volcano-sedimentary sequences near the SW margin of the graben, and confinement of
211 basaltic aeromagnetic fabrics to the hanging wall of the buried Mwanza Fault segment suggest the
212 presence of Mesozoic rift deposits beneath the Cenozoic sediments in the southwestern half of the
213 graben (Kolawole et al., 2022). Depth-to-magnetic basement estimates suggest that the present-day

214 NE border fault, Thyolo-Muona-Ruo Fault system may have accrued a larger post-Mesozoic vertical
215 displacement (ca. 1.5 km) than the the SW border fault, the Panga Fault (< 200 m) (Kolawole et al.,
216 2022). Despite up to 3 km erosion of the early rift sediments during the Mesozoic rifting phases (Bicca
217 et al., 2019), the present-day cumulative sediment thickness along the graben axis is estimated to be at
218 least 2.4 km (Kolawole et al., 2022). This suggests a possible Cenozoic strain accommodation along
219 the graben axis prior to the apparent ‘abandonment’ and burial of the southern Mwanza Fault.

220 The N-to-NNE-trending Nsanje Graben is located south of the Lower Shire Graben, and it defines
221 the northern continuation of the Urema Graben system of Mozambique (Figure 2; Pfaffling et al.,
222 2009). The graben is bounded to the west by the Nsanje Fault, and to the east by the Ndidi Fault
223 (Figure 3a). Both the Nsanje and Ndindi border faults crosscut the large-scale NE-trending
224 metamorphic fabrics of the host Precambrian basement (Bloomfield, 1958; Kolawole et al., 2022;
225 Thomas et al., 2022), indicating a lack of large-scale basement inheritance on border fault
226 development. Geologic maps show widespread coverage of Quaternary sediments across the entire
227 graben, deposited in the Ndindi Marsh and floodplains of the Shire River (Figures 3b; Bloomfield,
228 1958; Choubert et al., 1988).

229 1.1.3. The Middle Shire and Nsanje Rift Interaction Zones

230 The Middle Shire RIZ, which represents the zone of transition from the Zomba Graben to the Lower
231 Shire Graben, is characterized by a rotation of the Precambrian metamorphic basement fabrics from
232 NNE-SSW trend in the Zomba Graben area to a NW-SE trend in the Lower Shire Graben (Kolawole
233 et al., 2021a). The Nsanje RIZ, which represents the zone of transition from the Lower Shire Graben
234 to the Nsanje Graben occurs at the NE-trending Lurio Shear Zone, an exhumed ductile shear zone
235 separating the Unango and Nampula terranes of the Precambrian Southern Irumide Belt (Figure S1;
236 Fritz et al., 2013; Kolawole et al., 2022; Thomas et al., 2022). The Middle Shire RIZ defines an
237 overlapping oblique divergent RIZ geometry in which the NNE/N-trending Malawi Rift is
238 propagating southwards into the NE shoulder of the NW-trending Lower Shire Graben, whereas the
239 Nsanje RIZ is a tip-to-tip oblique RIZ (‘convergent’ border fault polarity pattern) in which the Lower
240 Shire Graben has propagated southeast into the northern tip of the N-trending Nsanje Graben (Figure
241 3a).

242 In contrast to the Nsanje RIZ which shows very sparse surface exposures of the Precambrian
243 basement along the modern rift floor, the Middle Shire RIZ is dominated by widespread exposures of
244 the basement (Figures 3b, 4a-b, 4c-d). In the Middle Shire RIZ, the rift floor tilts westwards towards
245 the escarpments of the Lisungwe and Wamkurumadzi Faults (e.g., Figure 4a). In the Nsanje RIZ, the
246 rift floor also tilts to the southwest but there is no surface expression of faulting (Figures 3b, 4c-d,
247 S2). Longitudinal topographic relief profile of the rift axis shows that the Zomba Graben and Middle
248 Shire RIZ are at a higher structural elevation than the Nsanje Graben (Figure 4e). Thus, based on the
249 criteria of border fault connectivity, cross-over topographic and axial stream morphology, and
250 directionality of axial stream flow, the Middle Shire RIZ is interpreted to be a recently breached RIZ,
251 and the Nsanje Graben a breached RIZ that is undergoing rift coalescence (Kolawole et al., 2021a).

252

253 1.1.4. Modern Rift Basin Drainage Geomorphology

254 The southern Malawi-central Mozambique region is characterized by a tropical climate, in which dry
255 seasons generally extend from April to September (average annual rainfall of ~0.65 m at Tete), and
256 wet seasons from October to March (Garzanti et al., 2022). The modern landscape of the Zomba-
257 Lower Shire-Nsanje graben system is drained by the Shire River and its 18,000 km² catchment area
258 (Figure 3a). The south-flowing, ca. 490 km-long axial stream represents the largest river in Malawi, the
259 only outlet for Lake Malawi, and one of the major tributaries of the Zambezi River (Price, 1966;
260 Palamuleni et al., 2011; Dulanya, 2017). Zambezi River Delta represents one of the largest sediment
261 supply points into the Mozambique Channel arm of the Indian Ocean, highlighting the significance
262 of the Shire River for sediment contributions into the ocean basin depositional sink (Garzanti et al.,
263 2022). Although the Shire River represents the only modern fluvial link between Lake Malawi and the
264 Indian Ocean, the trunk stream is punctuated by major sediment sinks which includes Elephant Marsh
265 in the Lower Shire Graben and Ndindi Marsh in the Nsanje Graben (Figure 3a). The Elephant Marsh
266 and Ndindi Marsh represent wetlands that have developed in the axial depocenters of the Lower Shire
267 and Nsanje grabens, but are connected across the Nsanje RIZ, and the transition between the two
268 wetlands is defined by a zone of decrease in width of the wetland within the Nsanje RIZ (Figure 3b).

269 The river course is divided into the 'Upper Shire' section at ca. 500 m elevation in the Zomba Graben,
270 the 'Middle Shire' section in the Middle Shire RIZ where the river drops across a ca. 80 m escarpment
271 over 72 km distance, and the 'Lower Shire' section at ca. 45 - 50 m elevation in the Lower Shire Graben
272 (Figure 4e). The rectilinear planform geometry, the large-scale relief morphology of the longitudinal
273 elevation profile of the Middle Shire section, as well as the clustering of rapids and waterfalls (i.e.,
274 knickpoints) within the section (see Figure 4b) suggests that the Middle Shire section is not
275 equilibrated with the downstream sections of the stream profile (Dulanya, 2017; Kolawole et al., 2021a;
276 Dulanya et al., 2022). More importantly, in contrast to the axial stream profile within the Middle Shire
277 RIZ, the 'flat' longitudinal relief morphology and sinuous planform geometry of the axial stream across
278 the Nsanje RIZ (Figures 4d-e) suggests an equilibrated profile. These observations are also consistent
279 with the contrasts in the axial stream planform morphology between the two RIZs, whereby in the
280 Middle Shire RIZ, the axial stream exhibits significantly lower channel sinuosity and channel width in
281 contrast to the Nsanje RIZ (Kolawole et al., 2021a). Furthermore, the highly sinuous axial stream
282 planform morphology of the Lower Shire section generally continues southwards through the Nsanje
283 RIZ and the Nsanje Graben.

284 Investigation of the knickpoint initiation times in the Middle Shire River catchment suggested that the
285 Upper and Lower Shire were not integrated into a single south-flowing stream until around the Mid-
286 Pleistocene (Dulanya et al. 2022). The Middle Shire region is interpreted to have been an elevated
287 basement block that previously isolated the Lower Shire Graben from the Zomba Graben, at the time
288 of which the Lower Shire River section flowed south, and the Upper Shire hosted a lake (paleo-lake
289 Matope) that flowed north into Lake Malawi with alternating periods flooding of Lake Malawi into
290 the Zomba Graben (Dulanya, 2017). The subsequent integration of the axial stream across the Middle
291 Shire is likely to have been facilitated by the continued brittle deformation and down-faulting of the
292 Middle Shire basement by the tectonic interaction between the northwestward propagation of the
293 Thyolo Fault and possibly, a simultaneous propagation of the southern Zomba Graben faults
294 (Kolawole et al., 2021a). Thus, the structural breaching of the Middle Shire RIZ and the linkage of the
295 Zomba and Lower Shire grabens is inferred to have taken place as recent as the Mid Pleistocene,
296 relative to the Oligocene-Miocene initiation of Cenozoic rifting in the region (Dulanya et al., 2022).

297

298 **2. Methods**299 **2.1. Field Observations as Constraints on Rift Kinematics**

300 To constrain the kinematics of rifting in southern Malawi, we perform field investigations on the
 301 outcrops of border faults in the Lower Shire and Nsanje grabens (locations are ‘red stars’ in Figure
 302 3a). The natural observations of fault kinematics from the study area provide constraints on our
 303 numerical model (see section 2.2). Our fieldwork involved the collection of measurements of slip
 304 indicators on the slip surfaces of the border faults, which include strike and dip of fault surfaces, and
 305 the trend and plunge of highest quality slip stria on the surfaces. As for the Zomba Graben, we utilize
 306 published field measurements (from Wedmore et al., 2020b) taken along the largest intrabasinal fault
 307 in the basin, the Chingale Step Fault. These measurements (see Table 1) allow us to estimate a single
 308 kinematic strain tensor that is compatible with the kinematics of three rift basins in the current regional
 309 tectonic stress field. For this analysis, we utilize the FaultKin program (Marrett and Allmendinger,
 310 1990; Cladouhos and Allmendinger, 1993), adopting a uniform weight moment tensor summation.
 311 The program determines the principal strain directions using slip surfaces with known geometries and
 312 striae with known slip senses as input, while assuming that the deformation is coaxial. The analysis is
 313 a standard technique that produces a fault plane solution with two orthogonal nodal planes, the
 314 bisectors of which produce P- and T-axes of the incremental strain tensor. The P- and T-axes
 315 respectively represent the principal shortening (ϵ_3) and principal extension (ϵ_1) strain axes of the array
 316 of input faults.

317

318 **2.2. Modeling Landscape Evolution**

319 We use the FastScape algorithm (Braun and Willett, 2013) to solve the stream power law to estimate
 320 the response of surface processes to rift tip propagation in different RIZs. The FastScape code
 321 simulates bedrock river incision and deposition by (Yuan et al., 2019):

322

$$323 \quad \frac{\partial h}{\partial t} = U - KA_m S^n + \frac{G}{A} \int_A \left(U - \frac{\partial h}{\partial t} \right) dA \quad \text{where } h \geq h_{\text{base}} \quad (1)$$

$$324 \quad \frac{\partial h}{\partial t} = K_b \nabla^2 h + \int_A \left(\frac{U - \frac{\partial h}{\partial t}}{\partial x \partial y} \right) dA \quad \text{where } h < h_{\text{base}} \quad (2)$$

325

326 Where h and h_{base} is the elevation and elevation of rift lake, respectively, so Equation 1 and 2 represent
 327 the landscape evolution on the land and in the rift lake, t is time, U , A , S are uplift rate, drainage area,
 328 and local slope respectively. K and G reflect the lithology erodibility and deposition coefficient, K_b is
 329 the diffusion coefficient in the rift lake, presumably linearly corresponding to local slope, with a value
 330 of 30. m , n are poorly constrained constants that most depend on lithology and climate. We use $m =$
 331 0.5 , $n = 0.1$, $K = 4e-6$, $G = 1e-3$ based on previous work (e.g., Croissant and Braun, 2014, Guerit et
 332 al., 2019; Yuan et al., 2019).

333 The domain is 500 km by 500 km with cell size of 1 km² (Figures 5a-c). With a focus on the effects of
 334 rift segment tip propagation, we simplify the impacts of climate and lithology in the model and assume
 335 a constant rainfall of 1m/yr in the study area and a homogenous lithology. We apply the fixed value
 336 boundary condition for the four borders. The model time is 10 Myr with a timestep of 1 kyr; and we
 337 present results for the 5 Myr and 10 Myr timesteps. The model domain contains three contiguous
 338 grabens: NNE-trending Rift 1 in the north, NW-trending Rift 2 in the center, and NNE-trending Rift
 339 3 in the south (Figure 5c). The orientation of each graben-bounding fault reflects the location of
 340 border faults in the Zomba Graben (southern Malawi Rift), Lower Shire Graben, and Nsanje Graben,
 341 thus defining an oblique overlapping divergent RIZ between rifts 1 and 2, and an underlapping oblique
 342 convergent RIZ between rifts 2 and 3 (Figure 5c). Based on field observations along the major faults
 343 of the Zomba - Lower Shire - Nsanje graben system (see section 3.1; Figures 6a-h), we impose a
 344 normal faulting tectonic stress regime on each border fault in the model, such that each model rift
 345 basin undergoes orthogonal extension. The displacement of graben-bounding (border) normal faults
 346 is added as time-dependent uplift fields on topography. The maximum displacement, posted at the
 347 center of each fault, is 0.8 mm/yr and it decreases to zero at the tips of the faults, following a sinusoidal
 348 curve. The half-extension rate and tip growth rate are 1 mm/yr and 5 mm/yr, respectively for all
 349 border faults in the study area (Figure 4), based on the observed low extension rate of 2.2 mm/yr
 350 (Stamps et al., 2018). Positive displacement indicates uplift and negative displacement indicates
 351 subsidence; the background displacement rate in the model is 0.03 mm/yr (Figures 5a-b). In the
 352 model, each rift propagates bi-directionally. Thus, following the convention of Kolawole et al. (2021),
 353 since Rift 1 is located in the flank of Rift 2 in our model setup, Rift 1 serves as the propagator and
 354 Rift 2 the receiver segment across their intervening RIZ, whereas, at the underlapping oblique RIZ,
 355 both rifts 1 and 2 serve as propagator and receiver segments. Note that during the model run, the
 356 underlapping oblique convergent RIZ evolved into a tip-to-tip oblique RIZ geometry.

357

358 2.3. Modeling Static Tectonic Stress Distribution

359 Although the FastScape algorithm can project a topography at the end of a model run, it is limited in
 360 that it cannot resolve the static stress field associated with tectonic deformation. This is relevant for
 361 understanding the influence of compounding stress distribution on the displacement field observed
 362 in the landscape evolution model. Thus, we simulate the static Coulomb stress distribution across the
 363 modeled RIZ geometries, using the same input parameters of model domain size, fault geometry, and
 364 kinematics as in the landscape evolution model, and we implement the simulation in Coulomb 3.3
 365 available from USGS website (Toda et al., 2005; Lin, and Stein, 2004). The software utilizes an elastic
 366 half-space model to calculate static stress changes in space and time within a model domain due to
 367 slip on a given source fault. The general Coulomb stress change formulation is as follows:

368

$$369 \Delta\sigma_c = \Delta\tau_s + \mu'\Delta\sigma_n \quad (3)$$

370

371 Where $\Delta\sigma_c$ is the Coulomb stress change, $\Delta\tau_s$ is the shear stress change, and $\Delta\sigma_n$ is the normal
 372 (clamping) stress change on receiver normal faults due to slip on a source normal fault, and μ' is the

373 effective coefficient of friction on the faults. We use μ' of 0.55, appropriate for the southern Malawi
374 region (Williams et al., 2019), and fault rupture depth of 5 km. We use the total fault slip in 5 Myr as
375 prescribed displacement on fault plane and model cases involving the activation of each border fault
376 as the source fault while other faults act as the receiver faults; then, we model a single case in which
377 all the border faults are the source faults (i.e., all rupture in the same event) and calculate stress change
378 on N-S strike faults with a rake of -90. For simplicity, each fault is represented as a single rectilinear
379 planar surface. By implementing the static stress model, we can assess the predominant type of
380 Coulomb stress change (i.e., positive or negative) that is transferred into an oblique overlapping
381 divergent rift interaction zone area versus tip-to-tip rift interaction zone.

382

383 2.4. Model Limitations

384 The active northeastern border fault system of the Lower Shire Graben (Thyolo-Muona-Ruo Fault
385 System) is characterized by a staggered, side-stepping geometry that developed over multiple rift
386 phases (Kolawole et al., 2022; Figures 3a-b). Similarly, a major strand of the western border fault
387 system of the Zomba Graben (Lisungwe Fault) shows zig-zag geometry (Figures 3a-b). However, for
388 simplicity, we implemented this fault system as a single planar through-going fault in our model (Figure
389 5c). We assume the modeled faults have a uniform tip propagation and extension rates due to lack of
390 constants on the timing and rate of fault slip rates. We note a limitation of the poor constraints of
391 fault slip rates in southern Malawi and the shorter duration of model tectonic extension versus nature.
392 We note that although our model uses a constant rainfall rate throughout the model run, paleoclimate
393 studies in the region (e.g., Scholz et al., 2007; Beuning et al., 2011; Konecky et al., 2011; Dulanya et
394 al., 2014) show records of alternating wet and dry periods in as low as 100-year intervals. The limited
395 constraints on fault slip rates, rainfall rates, and the paleotopographic (pre-rift) variations might have
396 resulted in the mismatch between the absolute values of surface elevation in southern Malawi and
397 those in our model results.

398 We do not implement the NNW-rotation of the northwestern tip of the Thyolo Fault as it is found
399 to have been controlled by the Precambrian basement metamorphic fabrics (Kolawole et al., 2021a).
400 We also acknowledge that the static Coulomb stress change model only assumes a single instance of
401 slip involving the rupture of an entire border fault and does not capture the very complex interactions
402 of border and intrabasinal fault segments over the many cycles of earthquake activity in active rift
403 basins (e.g., Njinju et al., 2022).

404

405 3. Results

406 3.1. Fault Kinematics along the Zomba – Lower Shire - Nsanje Graben System

407 Field observations of fault-slip striae on exposed fault surfaces in the Zomba, Lower Shire, and Nsanje
408 grabens (Table 1; Figures 6a-g) show a strong component of normal slip on the faults, but with the
409 Nsanje data showing a relatively high obliquity. This is given by the 301°/52° striae (average
410 trend/plunge) on the Zomba Fault slip surface (189°/54° strike/dip; Wedmore et al., 2020b; Figures
411 8a-b), 231°/80° striae (trend/plunge) on the Thyolo Fault slip surface (160°/69°SW strike/dip;
412 Figures 6c-d), and 193°/44° striae (trend/plunge) on the Nsanje Fault slip surface (059°/79°SE

413 strike/dip; Figures 6e-g). However, these slip vectors, altogether produce a kinematic strain tensor of
 414 $023.3^\circ/69.1^\circ$ P-axis and $260.3^\circ/11.8^\circ$ T-axis, suggesting a predominantly normal faulting regime,
 415 although with a very minor strike-slip component. The 260.3° (80.3°) (ENE-WSW) T-axis trend is
 416 parallel to the known regional geodetically resolved tectonic extension azimuth of $086^\circ \pm 5^\circ$ (Stamps
 417 et al., 2008, 2018; Figure 3a) and the regional σ_3 stress direction of $072^\circ \pm 14^\circ$ from earthquake focal
 418 mechanism inversion (Williams et al., 2019). Similarly, the strain tensor solution is consistent with the
 419 largely normal faulting style of focal mechanism solutions of the recent earthquakes in the Nsanje RIZ
 420 (i.e., northern tip of the Nsanje Graben and southeastern tip of the Lower Shire Graben) and those
 421 in the Middle Shire RIZ (i.e., southern tip of the Zomba Graben) (Figures 3a-b). These results
 422 constrain the normal slip kinematics imposed on the faults in our landscape evolution model.

423

424 Table 1. Field data on slip vectors on border faults used for the kinematic tensor calculation.

Rift Basin	Border Fault	Strike/Dip	Plunge/Trend	Source
Zomba Graben	Chingale Step F.	$189^\circ/54^\circ$	$52^\circ/301^\circ$	Wedmore et al. (2020b)
Lower Shire Graben	Thyolo F.	$160^\circ/69^\circ$	$80^\circ/231^\circ$	This study
Nsanje Graben	Nsanje F.	$059^\circ/79^\circ$	$44^\circ/193^\circ$	This study

425

426

427 3.2. Overlapping Oblique RIZ: Model Displacement Field, Rift Topography, and 428 Drainage Morphology

429 After 5 Myr of model run, Rift 1 had propagated into the footwall of Rift 2 and the western border
 430 fault of Rift 1 is hard-linked with the northeastern border fault of Rift 2 across their intervening
 431 overlapping oblique RIZ (Figure 7a). The integrated fault displacement rate fields represent
 432 distribution of rift basin subsidence and flank uplift in RIZs. Particularly, Rift 1 is characterized by
 433 uniform displacement ellipses on its two border faults with up to 0.12 mm/yr footwall uplift rate, ca.
 434 0.2 mm/yr maximum hanging wall subsidence rate. At the overlapping RIZ, the southern tip of Rift
 435 1 extends into a narrow region that is dominated by background displacement rate of ca. 0.03 mm/yr
 436 or less. To the south of the RIZ, the northeastern border fault of Rift 2 shows a more pronounced
 437 hanging wall subsidence rate of >0.32 mm/yr. At the region of hard-linkage with the western border
 438 fault of Rift 1, the fault shows a localized zone of significant displacement rate at the western margin
 439 of the RIZ, defined by the region of fault intersection. More specifically, the localized subsidence
 440 occurs at the intersection of the southern extension of Rift 1's western border fault with the
 441 northwestern extension of Rift 2's northeastern border fault. Also, we note that, in general, Rift 2
 442 shows a greater axial subsidence rate (0.12 - 0.16 mm/yr) than Rift 1 (0.04 - 0.08 mm/yr).

443 The topography of RIZs is largely modified by the rift fault propagation, resulting in distinct
 444 topography and drainage pattern due to different types of RIZs. The surface topography of the
 445 overlapping oblique RIZ shows a narrow, uplifted block of up to 12 - 25 m, and the rift lake in Rift 2
 446 is deepest (ca. 40 m) to the south of the uplift (Figure 7b), consistent with the patterns in the
 447 displacement field map (Figure 7a). Although the drainage system is characterized by well-developed

448 rift lakes in rifts 1 and 2, the lakes remain disconnected across the overlapping RIZ (Figure 7c). These
449 results indicate that rifts 1 and 2 remain as isolated basins and their fluvio-lacustrine depositional
450 environments disconnected from each other. The cross-sectional view of rift structure across the RIZ
451 features a paired graben-half graben morphology in which there is a significantly exposed basement at
452 the rift floor with a graben structure to the west and half graben to the east (cross-section B-B' in
453 Figure 7d). Also, the section shows a thinner syn-rift cover (ca. 5 m) on the hanging wall of Rift 1's
454 eastern border fault and a thicker cover (up to ca. 40 m) on Rift 2's eastern border fault. In the region
455 of transition from the overlapping RIZ into Rift 2, the model shows the presence of a prominent
456 isolated depression at the top-basement surface which is also represented at the model top-syn-rift
457 sediment surface (Figure 9a); this represents the fault intersection-related depocenter that developed
458 early and continued to be active with progressive tectonic extension.

459 However, at the end of 10 Myr model run, the displacement field results show that the southward
460 propagating tip of Rift 1 has finally breached the overlapping RIZ, and the rifts are now structurally
461 hard-linked and coalesced across the RIZ (Figure 8a). In addition, both the surface topography and
462 drainage system (Figures 8b-c) show that the depositional environments of rift basins 1 and 2 are now
463 fully connected, and that a through-going axial rift floor has been established across the RIZ.
464 Moreover, the model results also show that the displacement rates on the border faults have now
465 decreased due to the overlapped uplift and subsidence, and that the zone of rift intersection is now
466 the focus of accelerated displacement (Figure 8a) and surface subsidence (Figure 8b). This zone of
467 focused displacement is the fault intersection depocenter bounded by faults that trend parallel to the
468 border faults of the interacting rift pair.

469

470 **3.3. Tip-to-Tip Oblique RIZ: Model Displacement Field, Rift Topography, and Drainage** 471 **Morphology**

472 In contrast to the overlapping RIZ, at the end of the 5 Myr model run, the rift tips of both Rift 2 and
473 Rift 3 have propagated towards each other and their axial depocenters have merged, forming a tip-to-
474 tip oblique RIZ (Figure 7a). The displacement field at the end of 5 Myr presents a different pattern to
475 the one of overlapping RIZ, where the border faults of Rift 3 commonly show a footwall uplift rate
476 of ca. 0.04 - 0.08 mm/yr with a maximum of 0.12 mm/yr, and a hanging wall subsidence rate of up
477 to 0.28 mm/yr. The basin shows an axial subsidence rate of 0.12 - 0.16 mm/yr, similar to Rift 2. More
478 importantly, a depocenter of 0.08 - 0.12 mm/yr subsidence rate extends from the axes of both rifts
479 and merges across the intervening tip-to-tip oblique RIZ. The model result shows the development
480 of localized subsidence at the zone of intersection of the southeastern extension of Rift 2's western
481 border fault with the northern extension of Rift 3's western border fault. Similarly, the southeastern
482 extension of Rift 2's northeastern border fault intersects with the northern extension of Rift 3's eastern
483 border fault (Figures 7a-b). These fault intersections represent a hard-linkage of the border faults,
484 forming a broad obtuse angled hanging wall sub-basin along the eastern margin of the RIZ and a
485 reflex angled sub-basin along the western margin. The reflex-angled linkage zone localized more
486 subsidence rate (up to 0.24 mm/yr) which decreases eastward to 0.08 in the obtuse-angled linkage
487 zone.

488 In the tip-to-tip RIZ, the basal surface topography features a wide low elevation area (ca. 12 m)
489 which deepens westward to ca. 30 m in the reflex-angled linkage zone (Figure 7b). The model drainage
490 map (Figure 7c) shows that the rift lakes of Rift 2 and Rift 3 are connected across the RIZ and deepen
491 from 12 m, westward to ca. 25 m in the western reflex-angled RIZ margin. In essence, the fluvio-
492 lacustrine depositional environments of the two rifts have linked and become open to one another.
493 The cross-section of the model tip-to-tip RIZ shows a west-dipping asymmetric graben morphology,
494 an absence of basement exposure, and a syn-rift sedimentary wedge that thickens from ca. 10 m at the
495 eastern margin to ca. 30 m at the western margin of the RIZ (cross-section C-C' in Figure 7d).

496 Along the axes of the model rift zones, the variation in top-synrift sedimentary surface relief mimics
497 that of the top-basement relief (Figure 9a). The syn-rift fill of model Rift 1 thins southwards and the
498 surface onlaps the basement exposures of the overlapping oblique RIZ. South of the RIZ, the model
499 surface drops steeply into Rift 2, at a location where the syn-rift cover sequence is thickest among all
500 three rifts. Interestingly, although the basement is buried across the tip-to-tip oblique RIZ, there exists
501 a broad upwarp at the top-basement above which the syn-rift sequence also defines a structural-high.
502 Also, the model tip-to-tip RIZ shows an isolated depression at the top-basement surface, but which
503 is non-existent at the model top-syn-rift sediment surface (Figure 9a); this represents the fault
504 intersection-related depocenter that developed early, and later became buried as the rift tips coalesced
505 across the RIZ.

506 Overall, prior to the coalescence of the rifts (10 Myr time step, Figure 8), the comparison of the along
507 axis relief morphology styles across the rift interaction zones in the initial model time step and the
508 study area (Figures 9a-b) shows a correlation of 'steep' topographic down-step across the overlapping
509 oblique RIZ and a gentle surface arching across the tip-to-tip RIZ. However, we note that the absolute
510 values of model surface displacement or elevation are not the same as those of the natural RIZ (Figures
511 9a-b), likely due to the poor constraints on the slip rate on border faults from the southern Malawi,
512 paleotopography, and possibly the imposed constant rainfall rates and duration of tectonic extension
513 in the models. The model predicts that there is no exposed basement across the tip-to-tip RIZ,
514 whereas natural observation shows the presence of a minor exposure of the basement within the RIZ
515 (Figure 9a). In addition, the model predicts that the rift depocenters are yet to link across the
516 overlapping RIZ, which contrasts with the Middle Shire RIZ across which the Shire River connects
517 the Zomba and Lower Shire grabens (Figures 3a-b).

518 The 10 Myr timestep shows a paleo-rift interaction zone across which rift coalescence is even more
519 advanced than it was at the 5 Myr timestep (Figures 8a-c). However, similar to the overlapping RIZ,
520 the tip-to-tip RIZ also shows a focusing of greater displacement rates and subsidence at the
521 intersection zone of the border faults and relatively lower displacement rates on the border faults
522 themselves (Figures 8a-b).

523

524 **3.4. Predicted Static Tectonic Stress Distribution across the RIZs**

525 The modeled stress field shows different patterns between tip-to-tip oblique RIZ and overlapping
526 oblique RIZ. In each case of single border fault rupture (Figures 10a-f), the regions of positive
527 Coulomb stress change (stress concentration) are at the tips of the faults, and the regions of negative
528 Coulomb stress change (stress relaxation) are in the hanging wall and footwall of the faults. Across

529 the overlapping RIZ, the lobes of stress concentration at the southern tips of Rift 1 border faults
530 (faults 1 and 2) generally extend into the footwall of Rift 2's northeastern border fault (Figures 10a-
531 b). The proximity of the southern tip of Rift 1's western fault (fault 2) to the northern tip of Rift 2's
532 northeastern fault (fault 3) allows for the repeat stress concentration events at the intersection zone
533 of the two border faults (Figures 10b-c). In contrast, the lobes of stress concentration at the southern
534 tip of Rift's eastern fault (fault 1) always only intersect with the large lobe of stress relaxation in the
535 footwall of Rift 2's northeastern fault (fault 3) (Figures 10a and 10c). Coulomb stress change transfer
536 to fault 3 due to slip on fault 1 shows a minor increase, mainly focused onto the central section of
537 fault 3's slip surface (3-D fault plane view in Figure 10a). In contrast, stress change transfer to fault 3
538 due to slip on fault 2 shows significant increase, and it is focused onto a large portion of northwestern
539 slip surface of fault 3 (3-d fault plane view in Figure 10b).

540 Across the tip-to-tip RIZ, all events of slip on any of Rift 2 and Rift 3's border faults (faults 3 to 6)
541 concentrate positive Coulomb stress changes in the RIZ (Figures 10c – 10f). The lobes of positive
542 stress change transfer due to slip on Rift 2's border faults (faults 3 and 4) extend onto the northern
543 tips of Rift 3's border faults (faults 5 and 6). Similarly, the lobes of positive stress change transfer due
544 to slip on faults 5 and 6 extend far onto the southwestern sections of Rift 2's faults 3 and 4. Overall,
545 the results can be summarized in a single model case where all the faults are activated as source faults
546 (Figure 10g), showing that the overlapping RIZ is largely a zone of stress relaxation and the tip-to-tip
547 RIZ a zone of compounded stress concentration.

548

549 4. Discussion

550 4.1. Comparison of Model Results with Natural Observations

551 4.1.1 Rift Interaction Zone Morphology

552 The general patterns of the surface and top-basement displacement and drainage morphology of the
553 model RIZs (Figures 9a-b) provide important insights relevant for understanding the structure and
554 pace of evolution of the Middle Shire RIZ and Nsanje RIZ. In the model, at sometime during the
555 propagation of the rifts (e.g., the 5 Myr time step), unlike the tip-to-tip RIZ, the rift floor of
556 overlapping RIZ retained widespread basement exposure, which is consistent with the current
557 widespread exposure of the Precambrian basement in the Middle Shire RIZ. Similarly, the broad
558 upwarp of the model syn-rift surface across the model tip-to-tip RIZ is collocated with the region of
559 upwarp in the long wavelength surface elevation across the Nsanje RIZ (Figures 9a-b). The model
560 shows an early coalescence of the rift axial lakes across the tip-to-tip RIZ, consistent with the extension
561 of a wetland drained by the Shire River across the Nsanje RIZ (Elephant and Ndindi Marshes, Figures
562 3a-b, 4d, 7c). Overall, in contrast to the tip-to-tip RIZ, the model predicts delayed coalescence of the
563 depositional environments across the overlapping oblique divergent RIZ (see disconnected rift lakes
564 in Figure 7c). In nature, although the depositional environments of the Zomba and Lower Shire
565 grabens are already connected (Shire River flows across the Middle Shire RIZ; Figure 3a), published
566 geomorphological analysis and knickpoint age estimates suggest a recent (Mid. Pleistocene) breaching
567 of the Middle Shire RIZ (Kolawole et al., 2021a; Dulanya et al., 2022) relative to the Late Oligocene
568 initiation of Cenozoic rifting in the region (Ojo et al., 2022a). Furthermore, both the model and natural

569 surface relief show the presence of the broad topographic ‘step’ from the Zomba Graben (Rift 1) into
570 the Lower Shire Graben (Rift 2) (Figures 9a-b).

571 The Bouguer gravity model of the Lower Shire Graben (WGM2012; Bonvalot et al., 2012; Figures 9b,
572 S3) shows a prominent rift-parallel gravity-low (ca. 25 mGal) anomaly near the center of the basin.
573 This anomaly has been observed in published airborne gravity map of the graben, interpreted to
574 represent a deep depocenter in the basin (Ngabu depocenter; Chisenga et al., 2018). This gravity-low
575 anomaly is collocated with a zone of localized >2.5 km subsidence on the hanging wall of the buried
576 southern Mwanza Fault along the axis of the Lower Shire Graben which records multiple phases of
577 tectonic extension (Kolawole et al., 2022). To the southeast, this gravity-low anomaly transitions into
578 a broad rift-orthogonal gravity-high (ca. 92 mGal) anomaly extending far into the Nsanje RIZ, which
579 then decreases again to <85 mGal in the Nsanje Graben (Figure 9b; Figure S3). Similarly, the along-
580 rift variation in the trend of the basement depth (Figure 9b) shows decreasing basement depths
581 towards the southeast. Both the aeromagnetic basement depth and gravity anomaly trends, together
582 suggest that the basement shallows into the Nsanje RIZ and deepens southwards into the Nsanje
583 Graben (Figure 9b). The results indicate that there exists a shallowly-buried basement-high beneath
584 the Nsanje RIZ, which is also predicted by the model in the tip-to-tip RIZ (Figure 9a).

585 Our interpretation of shallow basement burial in the Nsanje RIZ is reflected by the relatively small
586 vertical surface offset on the Ruo Fault (i.e., escarpment height; Figure S2), the broad upwarp of the
587 surface topographic relief across the RIZ (low-pass filtered SRTM plot in Figure 9b), and the restricted
588 basement exposure on the rift floor (Figures 3b, 4c-d, 9b). Interestingly, the Nsanje RIZ surface tilts
589 and deepens to the west without any visible surface fault scarp at the western margin of the RIZ
590 (Figures 4c-d, S2). We speculate that the westward tilting and deepening of the Nsanje RIZ is likely
591 due to the presence of a blind active NW-trending NE-dipping fault near the western margin of the
592 RIZ (see dashed fault in Figures 4c, S2). Potentially, higher slip rates on this blind fault relative to the
593 Ruo Fault could have created the apparent half-graben geometry of the RIZ, in which the Ruo Fault
594 hanging wall is on the ‘uplifted’ margin. The uplift of the northeastern margin of the RIZ relative to
595 the southwestern margin is highlighted by the presence of incising west-flowing transverse streams
596 that cut into the hanging wall of the Ruo Fault (map in Figure S2).

597 The inferred blind fault at the SW margin of the Nsanje RIZ may be responsible for some of the
598 earthquake clusters in the Nsanje RIZ (see Figure 3a) but likely remains blind due to sedimentation
599 rates outpacing the slip rate on the fault. Modern fault slip rates are generally considered to be low in
600 southern Malawi, but quantitative constraints are lacking (Williams et al., 2022). Also, there is no
601 quantitative constraint on sedimentation rates in the Lower Shire Graben due to the absence of high-
602 resolution subsurface imaging and well controls. However, the Shire River is a major river that drains
603 the region and channels large amounts of sediments into the Lower Shire and Nsanje grabens and
604 represents a major sediment contributor to the Zambezi River with the Mozambique Channel being
605 the being the sink of the river system (e.g., Dulanya et al., 2022; Garzanti et al., 2022). Furthermore,
606 the high sedimentation inference is supported by the broad swampy terrain of the southwestern
607 margin of the Nsanje RIZ (Figure 4d) being dominated by the Shire River flood plains and the
608 Elephant Marsh beneath which the fault is located (Figures 4c-d). In summary, at some time in the
609 past, the currently buried basement-high beneath the Nsanje RIZ sediments should have been a broad
610 exposed basement arch that may have isolated the Lower Shire Graben from the Nsanje Graben. With

611 progressive tectonic extension and rift propagation into the RIZ, this elevated basement block
612 subsequently experienced down-faulting, erosion, and burial; a process which facilitated the structural
613 breaching of the RIZ and linkage of the two rift basins (Kolawole et al., 2021a).

614

615 4.1.2 Significance of Fault Intersection for the Deformation of Rift Interaction Zones

616 The landscape evolution model results predict a localized zone of elevated displacement rates and
617 associated basement subsidence at the western margin of the overlapping divergent RIZ, and another
618 one at the western margin of the tip-to-tip oblique RIZ, both colocated with regions of fault
619 intersection (Figures 7a-b, 7d, and 9a). We interpret this modeled subsidence to be consistent with the
620 development of isolated fault-bounded depocenters in the Middle Shire RIZ and the potential
621 presence of a blind high-strain fault in the western margin of the Nsanje Graben. Near the western
622 margin of the Middle Shire RIZ, the surface geology shows the presence of a ca. 17 km² isolated
623 depocenter of Quaternary sediments, herein referred to as the ‘Neno depocenter’ (Figures 3b). This
624 localized depocenter is elongate, NW-trending, and fault-bounded. It sits at the intersection of the
625 southern extension of the NNE-trending Lisungwe Fault and a NW-trending fault that trends parallel
626 to the Thyolo border fault of the Lower Shire Graben (Figure 3b). The basement subsidence is caused
627 by overlapped and enhanced displacement of rift faults, implying the possible control on the formation
628 of its natural equivalent, the Neno depocenter. Moreover, the topographic surface of the depocenter
629 is relatively ‘smoother’ than the surrounding basement-dominated topography (Figure 3a), consistent
630 with a dominance of unconsolidated sediments.

631 Just south of the Neno depocenter, in Majete, we observe an even broader (ca. 42 km²) NW-trending
632 fault-bounded area with similar surface smoothness as the Neno depocenter, possibly representing an
633 incipient localized depocenter (Figures 3b-c). This potential depocenter in Majete sits at the
634 intersection of the southern extension of the NNE-trending Wamkurumadzi Fault and a NW-trending
635 fault parallel to the Thyolo Fault. The cross-sectional topographic relief profile of the RIZ (Figure 4a)
636 shows a ca. 35 km-wide graben structure, with a surface that deepens towards the Lisungwe and
637 Wamkurumadzi faults to the west and is bounded to the east by a system of NW-trending faults.
638 Generally, both antithetic and synthetic fault linkage create localized amalgamated depocenters on the
639 hanging wall of both faults (synthetic interaction, Figures 7a, 8a) or in the hanging wall of the dominant
640 fault segment (antithetic interactions; Figures 7a, 7d inset; Duffy et al., 2015). The depocenters are
641 often well represented as prominent anomalies in the throw-distance (T-x) profiles of the interacting
642 faults with their characteristic abrupt ‘throw steps’ (3-D sketch and T-x plots in Figure 7d inset; Duffy
643 et al., 2015). However, based on insights of fault intersection depocenters from our modeling results
644 (Figures 7-8), we interpret these isolated fault-bounded depocenters in the Middle Shire RIZ to be
645 distributed local subsidence zones that are controlled by the intersection and interaction of fault
646 segments extending from the Zomba and Lower Shire rifts into the RIZ. Notably, recent analog
647 models of linkage between obliquely-oriented rifts show linkage of antithetic faults at the propagating
648 fault tips (Schmid et al., 2023).

649 On the dominant dip of faults that host the fault intersection depocenters, we note that the
650 overlapping divergent RIZ model results present the fault intersection-related depocenter to be
651 localized on a NW-dipping fault; whereas natural observations show the isolated depocenters in the

652 Middle Shire RIZ to be localized on NE-dipping faults. We suggest that the inherited heterogeneity
653 of the pre-rift basement of the Middle Shire RIZ may play an important role in determining the
654 dominant fault dip direction, which our models are not designed to assess. Nevertheless, the model
655 results suggest that localities of fault intersection within deforming RIZs are zones that localize
656 subsidence where significant tectonic strain associated with progressive rift linkage may accumulate.
657 Further, these fault intersection zones are zones where strain is transferred between the interacting
658 rift tips as they propagate across a deforming RIZ. The early localization of subsidence in the model
659 tip-to-tip RIZ is facilitated by the early intersection of propagating border fault tips into the RIZ, and
660 the model predicts that even during the advanced stages of rift coalescence, the continued deepening
661 of the RIZ sub-basin is most intense in the location of the early fault intersection depocenter (Figure
662 7d). Thus, we suspect that westward deepening of the Nsanje RIZ could be indicative of either the
663 presence of a buried fault intersection-related localized depocenter or a NW-trending, NE-dipping
664 normal fault at the southwestern margin of the RIZ. This may possibly be facilitating the incursion of
665 wetlands (Elephant Marsh) from the Lower Shire Graben into the western margin of the Nsanje RIZ
666 (Figures 3a-b, 4c-d). Altogether, the landscape evolution model results and natural observations
667 suggest that after the structural breaching of a rift interaction zone (i.e. post-rift linkage), rift
668 coalescence is initiated by the localization of distributed incipient depocenters as overlapped hanging
669 wall subsidence. Such depocenters may preferentially develop at localities of fault-intersection within
670 the RIZ.

671

672 4.1.3 Tectonic Stress Transfer and Active Faulting in the Rift Interaction Zones

673 The seismicity patterns in the region reflect relatively greater clustering of earthquakes in the Nsanje
674 RIZ compared to the Middle Shire RIZ (Figures 3a-b). The clustered events in the Nsanje RIZ
675 includes a Mw 5.5 event and its aftershocks that likely ruptured the Ruo Fault and the northern
676 extension of the Nsanje and Ndindi faults. The largest magnitude events in the Nsanje RIZ (Mw 5.5
677 and Mw 4.9; source: USGS earthquake catalog) occurred near the eastern margin of the RIZ. The
678 focal mechanism nodal planes generally trend N-to-NNW and NW, the former being parallel to the
679 trend of the Nsanje Graben border faults (Nsanje and Ndindi faults), and the latter being parallel to
680 the trend of the Ruo border fault segment (Figures 3a-b). These seismicity patterns likely reflect a
681 more pronounced active crustal deformation with significant moment release, and a localization of
682 brittle strain within the Nsanje RIZ. Although instrument records show the occurrence of at least one
683 Mw>5 event in the Middle Shire RIZ (Figure 3a), the events seem relatively more sporadic than those
684 in the Nsanje RIZ.

685 The Coulomb static stress transfer models predict a concentration of positive Coulomb stress changes
686 within the tip-to-tip RIZ produced by normal slip on the rift border faults, which contrast the case of
687 overlapping oblique divergent RIZ where a collocation of positive and negative stress changes is
688 predicted (Figure 8). In essence, in the tip-to-tip RIZ, the propagating rift tips grow into a zone of
689 stress concentration within the RIZ, whereas, in the overlapping divergent RIZ, the propagating rift
690 tip grows into a zone of stress relaxation. These results highlight the significant role of border fault
691 dip polarity in determining how static stress changes are transferred across deforming RIZs. Indeed,
692 antithetic dips of interacting border faults inhibit stress concentrations, compared to synthetically
693 interacting border faults. The long-term compounding effect of stress relaxation in overlapping RIZs

694 suggests that such RIZs host a persistent stress shadow where strain relaxation dominates. Altogether,
695 these model results suggest that over the repeated cycles of fault slip events at the propagating rift
696 tips, the time-averaged brittle strain accumulation will likely be greater in tip-to-tip RIZs than in
697 overlapping divergent RIZs. Although the constraints on fault slip history is sparse, we can still
698 interpret that depending on RIZ geometry, a RIZ may localize compounding stress concentration,
699 favoring rapid rift linkage and coalescence as in the case of tip-to-tip RIZs, or may experience
700 compounding stress relaxation, favoring delayed rift coalescence, as in the case of overlapping
701 divergent RIZs.

702 The southern tip of the Zomba Fault appears to be ‘stagnated’ as it does not extend across the entire
703 Middle Shire RIZ (Figure 3a) relative to the western border fault system of the Zomba Graben
704 (Lisungwe-Wamkurumadzi fault system) which has propagated close to and is soft-linked with the
705 northeastern border fault of the Lower Shire Graben (Thyolo Fault, and its subsidiary footwall faults)
706 (Figure 3a). We suggest that the attainment of hard linkage between the Lisungwe-Wamkurumadzi
707 and Thyolo faults can be explained by positive Coulomb stress change transfer onto the Thyolo Fault
708 surface due to slip on the Lisungwe-Wamkurumadzi fault system. The Coulomb stress change transfer
709 calculations show that slip on the Zomba Fault is not able to transfer significant positive stress change
710 onto the Thyolo Fault plane across the overlapping RIZ (3-d plot in Figure 10a). In contrast, the
711 proximity of the tips of fault 2 (representing Lisungwe-Wamkurumadzi fault system) and fault 3
712 (representing Thyolo Fault) predicts compounding stress concentration in the area between the
713 northwestern end of the Thyolo Fault and southern ends of the Lisungwe and Wamkurumadzi faults
714 (Figures 10a-b). Thus, the interaction of the fault tips allows the localization of brittle deformation,
715 facilitating the northwestward propagation of the Thyolo Fault and breaching of the RIZ. The two
716 fault systems are hard-linked by a cluster of NW-to-NNW-trending fault clusters, guided by the NW-
717 SE to NNW-SSE rotation of the pre-rift basement metamorphic fabrics (Kolawole et al., 2021a).

718

719 **4.2. Controls of Rift Interaction Zone Geometry on Early vs Delayed Rift Coalescence**

720 The striking contrast in the stages of evolution of the two model RIZs at the end of the 5 Myr (relative
721 to the 10 Myr) model runs, and the observations of present-day natural rift morphology at the Middle
722 Shire and Nsanje RIZs (e.g., Figures 9a-b) provide compelling evidence for a difference in the pace of
723 rift linkage with variation in RIZ geometry. This interpretation agrees with the predicted patterns of
724 crustal stress distribution across overlapping divergent (antithetic border fault interactions) and tip-
725 to-tip RIZs (synthetic border fault interactions) (Figure 10). The results predict delayed rift coalescence
726 across an overlapping divergent RIZ and demonstrate that it can be explained by the propagation of
727 rift tips into a persistent stress relaxation zone in the RIZ. Although the persistent footwall uplift of
728 the flank of the ‘receiver’ rift segment (e.g., Rift 2) inhibits subsidence across the overlapping divergent
729 RIZ, the kinematic opening direction of such a rift induces compression that acts normal to the
730 direction of growth of the ‘propagator’ rift segment tip (i.e., southern tip of Rift 1). Thus, compression
731 normal to rift tip propagation direction can also contribute to a delayed advancement of the
732 ‘propagator’ rift tip into the overlapping divergent RIZ. This is consistent with observations of
733 stagnation of propagating mid-oceanic ridges by compressive tectonic loading in the direction of ridge
734 propagation (Le Pourhiet et al., 2018).

735 Strong crustal blocks beneath a RIZ, either crustal-scale or only in the lower-crust, can inhibit rapid
736 propagation of a rift tip (Van Wijk and Blackman, 2005; Le Pourhiet et al., 2018). However, this is not
737 likely to be the case in our study area as basement geologic maps (e.g., Bingen et al., 2009; Fritz et al.,
738 2013; Thomas et al., 2022) and large-scale basement metamorphic fabric trends (Kolawole et al.,
739 2021a, 2022) of the region do not show the presence of a discrete basement block separating the
740 southern Malawi Rift from the Lower Shire Graben. However, numerical models show that significant
741 activation of rift stalling by lower crustal rheological blocks is in fact, most significantly activated when
742 there is compressive tectonic loading ahead of the propagating rift tip (Le Pourhiet et al., 2018). Also,
743 regional weak lower crust beneath interacting rifts and their intervening RIZ may also delay rift linkage,
744 and low surface erosional efficiency may delay the coalescence of depositional environments of
745 interacting rifts (Wolf et al., 2022). Nonetheless, although the Nsanje RIZ developed over the NE-
746 trending Precambrian Lurio Shear Zone (Kolawole et al., 2022), there is no evidence on the lower
747 crustal property of the shear zone that might suggest that it is significantly stronger than the lower
748 crust of the Middle Shire RIZ. Therefore, we cannot strongly claim that some unknown lower crustal
749 character influenced the delayed rift linkage and coalescence across the Middle Shire RIZ.

750 Thus, we argue that in non-volcanic active rift settings, the geometry of rift interaction zones strongly
751 influences the pace of rift linkage and coalescence by modulating the overall static stress distribution
752 and tectonic loading patterns across the RIZ. As a consequence, RIZ geometry may modulate the
753 evolution of the syn-rift depositional environment, as well as patterns of landscape evolution in
754 actively deforming zones of rift interaction. This was initially speculated in Kolawole et al. (2021)
755 based on conceptual understanding of a transition from a surface topographic basement-high RIZ
756 into a 'flat' sediment-covered area defining a paleo-RIZ. It was also speculated that paleo-RIZs can be
757 identified by the presence of buried large basement blocks at zones of lateral changes in the along-
758 trend geometry of a continental rift or rifted margin (Kolawole et al., 2021a). However, this current
759 study provides natural and model examples that validate these speculations, as well as a detailed
760 evaluation of how RIZ geometry may control the pace of transformation of a RIZ with progressive
761 tectonic deformation.

762 Models of rift propagation commonly test for the controls of extension direction (i.e., oblique versus
763 orthogonal) on the deformation patterns across rift interaction zones (e.g., Brune, 2014; Zwaan and
764 Schreurs, 2017; Zwaan et al., 2022). However, little is known of the control of the relationship between
765 obliquity of extension on the pace of lateral rift propagation and linkage of interacting rift segments.
766 Although our study is primarily focused on a rift zone with predominantly normal faulting kinematics
767 (Figure 6h; Williams et al., 2019), we note that it is also possible that the appreciable strike-slip
768 component of slip on the Nsanje Fault (Figure 6g) may have promoted the rapid lateral propagation
769 of the rift into the Nsanje RIZ. Overall, we think that the observations and model results in Middle
770 Shire and Nsanje RIZs can be applied to RIZs elsewhere. For example, the ca. 750 km-long Malawi
771 Rift and 730 km-long Tanganyika Rift exhibit greater rift lengths than many other rift segments in the
772 East African Rift System. The two rifts were proposed to have evolved over multiple pulses of lateral
773 propagation (e.g., Specht and Rosendahl 1989; Scholz et al., 2020; Kolawole et al., 2021a; Shaban et
774 al., 2023). The Kavala Island Ridge, buried beneath the central Tanganyika Rift, is an example of a
775 basement block at which rift segments define overlapping RIZ geometry, and in which their border
776 faults define a divergent overlapping transfer zone (Specht and Rosendahl 1989; Morley et al., 1990;
777 Muirhead et al., 2018; Shaban et al., 2023). This ridge is argued to be a long-lived structural-high in

778 the Tanganyika Basin, which served as a paleo-drainage divide during periods of lowstands (Scholz
779 and Rosendahl, 1988; Shaban et al., 2023). Such large structurally controlled paleo-drainage divides
780 commonly modulate biodiversity patterns in active continental rift environments (e.g., Russell et al.,
781 2012; Dommain et al., 2022), demonstrating the roles of RIZ evolution on sedimentary depositional
782 environment, landscape evolution, and floral and faunal speciation gradients.

783 Similarly, along the Malawi Rift, published maps of the basement topography (Specht and Rosendahl,
784 1989; Scholz et al., 2020) reveals the presence of a large 4,700 km² basement-block, the 'Likoma-
785 Lipichilli Block', buried beneath younger syn-rift sediments in the central section of the rift. This
786 basement block separates the northern Malawi Rift from the southern Malawi Rift and could have
787 represented a major structural-high on the paleo-topography of the rift, possibly serving as a paleo-
788 drainage divide during periods of low stands. For example, the block is collocated with an inferred
789 earlier termination zone of the northern Malawi Rift during the long-term southward growth of the
790 rift (Scholz et al., 2020).

791

792 **Conclusions**

793 We applied geologically constrained landscape evolution and static stress models to evaluate the
794 surface processes and stress state in two contiguous non-volcanic rift interaction zones of contrasting
795 end-member rift interaction zone (RIZ) geometries, the Zomba - Lower Shire - Nsanje graben system
796 at the southern branch of the East African Rift System. The Middle Shire RIZ is an overlapping
797 oblique divergent RIZ in which the NNE/N-trending southern Malawi Rift is propagating into the
798 NE shoulder of the NW-trending Lower Shire Graben, where widespread basement exposure
799 dominates the rift floor. The Nsanje RIZ is a tip-to-tip oblique RIZ in which the Lower Shire Graben
800 has propagated into the northern tip of the N-trending Nsanje Graben, where the rift floor is
801 dominated by widespread sediment deposition with minor basement exposure.

802 In general, the landscape evolution model results provide insights into the evolution of surface
803 morphology and rift structure across the RIZs in the study area. The model results show that with
804 progressive extension and tip growth, the overlapping oblique divergent RIZ maintains minor
805 basement down-throw and an unequilibrated axial stream profile, which contrasts the widespread
806 basement burial and equilibrated axial stream profile across tip-to-tip RIZ. Further, static tectonic
807 stress distribution models suggest compounding stress concentrations at tip-to-tip RIZs, thus implying
808 that brittle strain localization and rift coalescence is favored in such RIZs. In contrast, the model
809 predicts compounding stress relaxation at overlapping oblique divergent RIZs, favoring stalled rift
810 coalescence, and providing kinematic explanation on the distribution of deformation in these two
811 RIZs. These findings indicate that antithetically interacting border faults inhibit stress concentration
812 within RIZs, and that synthetically interacting border faults are stress concentrators within their
813 intervening RIZs. The results show that the kinematics of the rift border faults across the overlapping
814 divergent RIZ induces compression normal to the rift tip propagation direction, promoting delayed
815 advancement of the 'propagator' rift tip into the overlapping RIZ. Thus, we argue that in the absence
816 of magmatism, RIZ geometry strongly influences the pace of rift coalescence by modulating the spatial
817 distribution of tectonic stresses necessary to promote rift-linking deformation. The field observations
818 and model results in Middle Shire and Nsanje RIZs presented in this study provide a better

819 understanding of how the geometry rift interaction zones elsewhere may influence the pace of rift
820 linkage and coalescence.

821

822 **Acknowledgements**

823 We thank Elizabeth Catlos for the editorial handling of our paper, and reviewers Bailey Lathrop and
824 two anonymous reviewers for their comments and suggestions that have helped to improve the quality
825 of the manuscript. Thanks to Chikondi Chisenga for assisting during the field work. We also thank
826 the Columbia Climate School for providing the research funds that supported the field component of
827 this project.

828

829 **Author contributions**

830 F.K. and L.X. conceptualized the project. F.K. performed the fieldwork. L.X. conducted the numerical
831 modelling. F.K. and L.X. interpreted the results. F.K. wrote the manuscript. L.X. and Z.D. revised the
832 manuscript.

833

834 **Data Availability**

835 All the datasets supporting the analysis performed in this work are either already in public domain or
836 provided in the manuscript, and none are proprietary. Fastscape is available via zenodo (DOI:
837 10.5281/zenodo.4435110). Coulomb 3.3 is accessible from USGS
838 (<https://pubs.usgs.gov/of/2011/1060/>).

839

840 **References**

841 Aanyu, K. and Koehn, D. (2011). Influence of pre-existing fabrics on fault kinematics and rift
842 geometry of interacting segments: analogue models based on the Albertine Rift (Uganda), Western
843 Branch-East African Rift System. *Journal of African Earth Sciences*, 59(2-3), pp.168-184.

844 Agar, S.M. and Klitgord, K.D. (1995). Rift flank segmentation, basin initiation and propagation: a
845 neotectonic example from Lake Baikal. *Journal of the Geological Society*, 152(5), pp.849-860.

846 Barr, M.W.C., Brown, M.A. (1987). Precambrian gabbro–anorthosite complexes, Tete Province,
847 Mozambique. *Geol. J.* 22 (S2), 139–159.

848 Beuning, K. R. M., Zimmerman, K. A., Ivory, S. J., and Cohen, A. S. (2011). Vegetation response to
849 glacial–interglacial climate variability near Lake Malawi in the southern African tropics.
850 *Palaeogeography, Palaeoclimatology, Palaeoecology*, 303, 81–92.

- 851 Bicca, M.M., Jelinek, A.R., Philipp, R.P. and Jamal, D.L. (2019). Mesozoic-Cenozoic landscape
852 evolution of NW Mozambique recorded by apatite thermochronology. *Journal of Geodynamics*, 125,
853 pp.48-65.
- 854 Bingen, B., Jacobs, J., Viola, G., Henderson, I.H.C., Skår, Ø., Boyd, R., Thomas, R.J., Solli, A., Key,
855 R.M., Daudi, E.X.F. (2009). Geochronology of the Precambrian crust in the Mozambique belt in NE
856 Mozambique, and implications for Gondwana assembly. *Precambrian Res.* 170 (3–4), 231–255.
- 857 Bloomfield, K. (1958). The geology of the Port Herald area. *Bull. Geol. Surv. Malawi*, 9, Zomba.
- 858 Bloomfield, K. (1965). The Geology of the Zomba Area, *Bull. Geol. Surv. Malawi*, 16, 193 pp.
- 859 Bonvalot, S., Balmino, G., Briais, A., M. Kuhn, Peyrefitte, A., Vales, Biancale, R., Gabalda, G.,
860 Moreaux, G., Reinquin, F. Sarrailh, M. (2012). World Gravity Map, 1:50000000 map, Eds. : BGI-
861 CGMW-CNES-IRD, Paris.
- 862 Bosworth, W., 1985. Geometry of propagating continental rifts. *Nature*, 316(6029), pp.625-627.
- 863 Braun, J., & Willett, S. D. (2013). A very efficient $O(n)$, implicit and parallel method to solve the
864 stream power equation governing fluvial incision and landscape evolution. *Geomorphology*, 180, 170-
865 179.
- 866 Bosworth, W., 1985. Geometry of propagating continental rifts. *Nature*, 316(6029), pp.625-627.
- 867 Brune, S., 2014. Evolution of stress and fault patterns in oblique rift systems: 3-D numerical
868 lithospheric-scale experiments from rift to breakup. *Geochemistry, Geophysics, Geosystems*, 15(8),
869 pp.3392-3415.
- 870 Castaing, C. (1991). Post-Pan-African tectonic evolution of South Malawi in relation to the Karroo
871 and recent East African rift systems. *Tectonophysics*, 191(1-2), pp.55-73.
- 872 Chisenga, C., Dulanya, Z., and Yan, J. (2018). The structural re-interpretation of the Lower Shire Basin
873 using edge detection and gravity inversion methods of basement topography. *Journal of African Earth*
874 *Science*, 149, 280–290.
- 875 Chorowicz, J. (2005). The east African rift system. *J. Afr. Earth Sci.* 43 (1–3), 379–410.
- 876 Cladouhos, T.T. and Allmendinger, R.W., 1993. Finite strain and rotation from fault-slip data. *Journal*
877 *of Structural Geology*, 15(6), pp.771-784.
- 878 Coffield, D.Q. and Schamel, S., 1989. Surface expression of an accommodation zone within the Gulf
879 of Suez rift, Egypt. *Geology*, 17(1), pp.76-79.
- 880 Corti, G., van Wijk, J., Cloetingh, S. and Morley, C.K. (2007). Tectonic inheritance and continental
881 rift architecture: Numerical and analogue models of the East African Rift system. *Tectonics*, 26(6).
- 882 Croissant, T., & Braun, J. (2014). Constraining the stream power law: a novel approach combining a
883 landscape evolution model and an inversion method. *Earth surface dynamics*, 2(1), 155-166.
- 884 Daly, M.C., Chorowicz, J., Fairhead, J.D. (1989). Rift basin evolution in Africa: the influence of
885 reactivated steep basement shear zones. *Geol. Soc. Lond., Spec. Publ.* 44 (1), 309–334.

- 886 Daly, M.C., Green, P., Watts, A.B., Davies, O., Chibesakunda, F., Walker, R. (2020). Tectonics and
887 Landscape of the Central African Plateau, and their implications for a propagating Southwestern Rift
888 in Africa. *Geochem. Geophys. Geosyst.* 21.
- 889 Daly, M.C., Lawrence, S.R., Kimun'a, D., Binga, M. (1991). Late Palaeozoic deformation in central
890 Africa: a result of distant collision? *Nature* 350 (6319), 605–607.
- 891 Delvaux, D. (1989). The Karoo to recent rifting in the western branch of the East-African Rift System:
892 a bibliographical synthesis. In: Mus. Roy. Afr. Centr., Tervuren (Belg.), D'ept. G'col. Min., Rapp.
893 Ann, 1990, 1991, pp. 63–83.
- 894 Dommain, R., Riedl, S., Olaka, L.A., deMenocal, P., Deino, A.L., Owen, R.B., Muiruri, V., Müller, J.,
895 Potts, R. and Strecker, M.R., 2022. Holocene bidirectional river system along the Kenya Rift and its
896 influence on East African faunal exchange and diversity gradients. *Proceedings of the National*
897 *Academy of Sciences*, 119(28), p.e2121388119.
- 898 Duffy, O.B., Bell, R.E., Jackson, C.A.L., Gawthorpe, R.L. and Whipp, P.S., 2015. Fault growth and
899 interactions in a multiphase rift fault network: Horda Platform, Norwegian North Sea. *Journal of*
900 *Structural Geology*, 80, pp.99-119.
- 901 Dulanya, Z. (2017). A review of the geomorphotectonic evolution of the south Malawi rift. *Journal*
902 *of African Earth Sciences*, 129, pp.728-738.
- 903 Dulanya, Z., Croudace, I., Reed, J.M. and Trauth, M.H. (2014). Palaeolimnological reconstruction of
904 recent environmental change in Lake Malombe (S. Malawi) using multiple proxies. *Water SA*, 40(4),
905 pp.717-728.
- 906 Dulanya, Z., Gallen, S.F., Kolawole, F., Williams, J.N., Wedmore, L.N., Biggs, J. and Fagereng, Å.
907 (2022). Knickpoint morphotectonics of the Middle Shire River basin: Implications for the evolution
908 of rift interaction zones. *Basin Research*.
- 909 Ebinger, C.J., Deino, A.L., Drake, R.E. and Tesha, A.L. (1989). Chronology of volcanism and rift
910 basin propagation: Rungwe volcanic province, East Africa. *Journal of Geophysical Research: Solid*
911 *Earth*, 94(B11), pp.15785-15803.
- 912 Ebinger, C.J., Jackson, J.A., Foster, A.N. and Hayward, N.J. (1999). Extensional basin geometry and
913 the elastic lithosphere. *Philosophical Transactions of the Royal Society of London. Series A:*
914 *Mathematical, Physical and Engineering Sciences*, 357(1753), pp.741-765.
- 915 Ebinger, C.J., Rosendahl, B.R. and Reynolds, D.J., 1987. Tectonic model of the Malawi rift, Africa.
916 *Tectonophysics*, 141(1-3), pp.215-235.
- 917 Ebinger, C.J., Yemane, T., Harding, D.J., Tesfaye, S., Kelley, S. and Rex, D.C., 2000. Rift deflection,
918 migration, and propagation: Linkage of the Ethiopian and Eastern rifts, Africa. *Geological Society of*
919 *America Bulletin*, 112(2), pp.163-176.
- 920 Fazlikhani, H., Aagotnes, S.S., Refvem, M.A., Hamilton-Wright, J., Bell, R.E., Fossen, H., Gawthorpe,
921 R.L., Jackson, C.A.L. and Rotevatn, A., 2021. Strain migration during multiphase extension, Stord
922 Basin, northern North Sea rift. *Basin Research*, 33(2), pp.1474-1496.

- 923 Fossen, H. and Rotevatn, A., 2016. Fault linkage and relay structures in extensional settings—A
924 review. *Earth-Science Reviews*, 154, pp.14-28.
- 925 Fritz, H., Abdelsalam, M., Ali, K.A., Bingen, B., Collins, A.S., Fowler, A.R., et al. (2013). Orogen styles
926 in the East African Orogen: a review of the Neoproterozoic to Cambrian tectonic evolution. *J. Afr.*
927 *Earth Sci.* 86, 65–106.
- 928 Garzanti, E., Bayon, G., Dinis, P., Vermeesch, P., Pastore, G., Resentini, A., Barbarano, M., Ncube,
929 L. and Van Niekerk, H.J., 2022. The Segmented Zambezi Sedimentary System from Source to Sink:
930 2. Geochemistry, Clay Minerals, and Detrital Geochronology. *The Journal of Geology*, 130(3), pp.171-
931 208.
- 932 Guerit, L., Yuan, X. P., Carretier, S., Bonnet, S., Rohais, S., Braun, J., & Rouby, D. (2019). Fluvial
933 landscape evolution controlled by the sediment deposition coefficient: Estimation from experimental
934 and natural landscapes. *Geology*, 47, 853–856. <https://doi.org/10.1130/G46356.1>
- 935 Hargrove, U.S., Hanson, R.E., Martin, M.W., Blenkinsop, T.G., Bowring, S.A., Walker, N.,
936 Munyanyiwa, H. (2003). Tectonic evolution of the Zambezi orogenic belt: geochronological,
937 structural, and petrological constraints from northern Zimbabwe. *Precambrian Res.* 123 (2–4), 159–
938 186.
- 939 Heilman, E., Kolawole, F., Atekwana, E. A., and Mayle, M. (2019). Controls of Basement Fabric on
940 the Linkage of Rift Segments. *Tectonics* 38 (4), 1337–1366. doi:10.1029/2018tc005362.
- 941 Koehn, D., Aanyu, K., Haines, S., and Sachau, T. (2008). Rift nucleation, rift propagation and the
942 creation of basement micro-plates within active rifts. *Tectonophysics*, 458(1–4), 105–116.
- 943 Kolawole, F. (2020). The Roles of Structural Inheritance in Regions of Induced Seismicity and Active
944 Tectonics. PhD Dissertation, University of Oklahoma. <https://hdl.handle.net/11244/324859>
- 945 Kolawole, F., Atekwana, E.A., Láo-Dávila, D.A., Abdelsalam, M.G., Chindandali, P.R., Salima, J.,
946 Kalindekafe, L. (2018). Active deformation of Malawi rift's north basin Hinge zone modulated by
947 reactivation of preexisting Precambrian Shear zone fabric. *Tectonics* 37 (3), 683–704.
- 948 Kolawole, F., Firkins, M.C., Al Wahaibi, T.S., Atekwana, E.A. and Soreghan, M.J. (2021a). Rift
949 interaction zones and the stages of rift linkage in active segmented continental rift systems. *Basin*
950 *Research*, 33(6), pp.2984-3020.
- 951 Kolawole, F., Phillips, T.B., Atekwana, E.A. and Jackson, C.A.L. (2021b). Structural inheritance
952 controls strain distribution during early continental rifting, Rukwa Rift. *Frontiers in Earth Science*,
953 p.670.
- 954 Kolawole, F., Vick, T., Atekwana, E.A., Laó-Dávila, D.A., Costa, A.G. and Carpenter, B.M. (2022).
955 Strain localization and migration during the pulsed lateral propagation of the Shire Rift Zone, East
956 Africa. *Tectonophysics*, 839, p.229499.
- 957 Konecky, B. L., Russell, J. M., Johnson, T. C., Brown, E. T., Berke, M. A., Werne, J. P., and Huang,
958 Y. (2011). Atmospheric circulation patterns during late Pleistocene climate changes at Lake Malawi,
959 Africa. *Earth and Planetary Science Letters*, 312, 318–326.

- 960 Koopmann, H., Brune, S., Franke, D. and Breuer, S., 2014. Linking rift propagation barriers to excess
961 magmatism at volcanic rifted margins. *Geology*, 42(12), pp.1071-1074.
- 962 Laó-Dávila, D.A., Al-Salmi, H.S., Abdelsalam, M.G. and Atekwana, E.A., 2015. Hierarchical
963 segmentation of the Malawi Rift: The influence of inherited lithospheric heterogeneity and kinematics
964 in the evolution of continental rifts. *Tectonics*, 34(12), pp.2399-2417.
- 965 Le Pourhiet, L., Chamot-Rooke, N., Delescluse, M., May, D.A., Watremez, L. and Pubellier, M., 2018.
966 Continental break-up of the South China Sea stalled by far-field compression. *Nature Geoscience*,
967 11(8), pp.605-609.
- 968 Lin, J. and R.S. Stein, 2004, Stress triggering in thrust and subduction earthquakes, and stress
969 interaction between the southern San Andreas and nearby thrust and strike-slip faults, *Journal of*
970 *Geophysical Research*, v. 109, B02303, doi:10.1029/2003JB002607.
- 971 Marrett, R. and Allmendinger, R.W., 1990. Kinematic analysis of fault-slip data. *Journal of structural*
972 *geology*, 12(8), pp.973-986.
- 973 McClay, K. and Khalil, S., 1998. Extensional hard linkages, eastern Gulf of Suez, Egypt. *Geology*,
974 26(6), pp.563-566.
- 975 McClay, K.R., Dooley, T., Whitehouse, P. and Mills, M., 2002. 4-D evolution of rift systems: Insights
976 from scaled physical models. *AAPG bulletin*, 86(6), pp.935-959.
- 977 Molnar, N.E., Cruden, A.R. and Betts, P.G., 2019. Interactions between propagating rifts and linear
978 weaknesses in the lower crust. *Geosphere*, 15(5), pp.1617-1640.
- 979 Morley, C.K., 1995. Developments in the structural geology of rifts over the last decade and their
980 impact on hydrocarbon exploration. *Geological Society, London, Special Publications*, 80(1), pp.1-32.
- 981 Morley, C.K., Wescott, W. A., Harper, R. M., and Cunningham, S. M. (1999). *Geology and Geophysics*
982 *of the Rukwa Rift. Geoscience of Rift Systems-Evolution of East Africa. AAPG Stud. Geology*. 44,
983 91–110.
- 984 Muirhead, J.D., Wright, L.J. and Scholz, C.A., 2019. Rift evolution in regions of low magma input in
985 East Africa. *Earth and Planetary Science Letters*, 506, pp.332-346.
- 986 Nelson, R. A., Patton, T. L., and Morley, C. K. (1992). Rift-segment interaction and its relation to
987 hydrocarbon exploration in continental rift systems (1). *AAPG Bulletin*, 76(8), 1153–1169.
- 988 Neuharth, D., Brune, S., Glerum, A., Heine, C., and Welford, J.K. (2021). Formation of continental
989 microplates through rift linkage: Numerical modelling and its application to the Flemish Cap and Sao
990 Paulo Plateau. *Geochemistry, Geophysics, Geosystems*, 22, 1–22.
- 991 Njinju, E.A., Atekwana, E.A., Stamps, D.S., Abdelsalam, M.G., Atekwana, E.A., Mickus, K.L.,
992 Fishwick, S., Kolawole, F., Rajaonarison, T.A. and Nyalugwe, V.N. (2019a). Lithospheric structure of
993 the Malawi Rift: Implications for magma-poor rifting processes. *Tectonics*, 38(11), pp.3835-3853.

- 994 Njinju, E.A., Kolawole, F., Atekwana, E.A. (2022). Coseismic static stress transfer between
995 propagating faults promotes intra-rift faulting: Insights from the 2009 Mw 6.0 and 2014 Mw 5.2
996 Karonga Earthquakes, Malawi Rift. AGU Fall meeting abstract #T17a-01.
- 997 Njinju, E.A., Kolawole, F., Atekwana, E.A., Stamps, D.S., Atekwana, E.A., Abdelsalam, M. G.,
998 Mickus, K.L. (2019b). Terrestrial heat flow in the Malawi Rifted Zone, East Africa: implications for
999 tectono-thermal inheritance in continental rift basins. *J. Volcanol. Geotherm. Res.* 387, 106656.
- 1000 Ojo, O., Thomson, S.N., Laó-Dávila, D.A. (2022a). Neogene–Quaternary Initiation of the Southern
1001 Malawi Rift linked to reactivation of the Carboniferous–Jurassic Shire Rift. *ESSOAr Preprint*.
1002 <https://doi.org/10.1002/essoar.10511357.1>.
- 1003 Ojo, O.O., Ohenhen, L.O., Kolawole, F., Johnson, S.G., Chindandali, P.R., Atekwana, E.A. and Laó-
1004 Dávila, D.A. (2022b). Under-displaced normal faults: Strain accommodation along an early-stage rift-
1005 bounding fault in the Southern Malawi Rift. *Frontiers in Earth Science*, 10.
- 1006 Palamuleni, L.G., Ndomba, P.M. and Annegarn, H.J., 2011. Evaluating land cover change and its
1007 impact on hydrological regime in Upper Shire River catchment, Malawi. *Regional Environmental*
1008 *Change*, 11(4), pp.845-855.
- 1009 Patton, T.L., Moustafa, A.R., Nelson, R.A. and Abdine, S.A., 1994. Tectonic evolution and structural
1010 setting of the Suez rift: chapter 1: Part I. Type basin: Gulf of Suez.
- 1011 Pfaffling, A., Monstad, S., Groom, R.W. and Rudd, J., 2009. Airborne-EM hydrocarbon mapping in
1012 Mozambique. *ASEG Extended Abstracts*, 2009(1), pp.1-6.
- 1013 Price, T., 1966. Shire, Shirwa, and Nyasa. *The Society of Malawi Journal*, pp.15-19.
- 1014 Ragon, T., Nutz, A., Schuster, M., Ghienne, J. F., Ruffet, G., and Rubino, J. L. (2019). Evolution of
1015 the Northern Turkana Depression (East African Rift System, Kenya) during the Cenozoic Rifting:
1016 New Insights from the Ekitale Basin (28-25.5 Ma). *Geol. J.* 54 (6), 3468–3488. doi:10.1002/gj.3339.
- 1017 Rosendahl, B.R., 1987. Architecture of continental rifts with special reference to East Africa. *Annual*
1018 *Review of Earth and Planetary Sciences*, 15(1), pp.445-503.
- 1019 Rosendahl, B.R., Reynolds, D.J., Lorber, P.M., Burgess, C.F., McGill, J., Scott, D., Lambiase, J.J. and
1020 Derksen, S.J., 1986. Structural expressions of rifting: lessons from Lake Tanganyika, Africa. *Geological*
1021 *Society, London, Special Publications*, 25(1), pp.29-43.
- 1022 Russell, J.M., Cohen, A.S., Johnson, T.C. and Scholz, C.A., 2012. Scientific drilling in the East African
1023 Rift Lakes: A strategic planning workshop. *Scientific Drilling*, 14, pp.49-54.
- 1024 Rotevatn, A., Kristensen, T., Ksienzyk, A., Wemmer, K., Henstra, G., Midtkandal, I., Grundvåg, S.A.,
1025 Andresen, A., 2018. Structural inheritance and rapid rift-length establishment in a multiphase rift: the
1026 East Greenland rift system and its Caledonian orogenic ancestry. *Tectonics* 37, 1858–1875.
- 1027 Ryan, W. B. F., S.M. Carbotte, J. Coplan, S. O'Hara, A. Melkonian, R. Arko, R.A. Weissel, V. Ferrini,
1028 A. Goodwillie, F. Nitsche, J. Bonczkowski, and R. Zemsky (2009), Global Multi-Resolution
1029 Topography (GMRT) synthesis data set, *Geochem. Geophys. Geosyst.*, 10, Q03014.

- 1030 Sachau, T., Koehn, D., Stamps, D.S. and Lindenfeld, M., 2016. Fault kinematics and stress fields in
1031 the Rwenzori Mountains, Uganda. *International Journal of Earth Sciences*, 105, pp.1729-1740.
- 1032 Sander, S. and Rosendahl, B.R., 1989. The geometry of rifting in Lake Tanganyika, east Africa. *Journal*
1033 *of African Earth Sciences (and the Middle East)*, 8(2-4), pp.323-354.
- 1034 Saria, E., Calais, E., Stamps, D.S., Delvaux, D. and Hartnady, C.J.H., 2014. Present-day kinematics of
1035 the East African Rift. *Journal of Geophysical Research: Solid Earth*, 119(4), pp.3584-3600.
- 1036 Schmid, T.C., Brune, S., Glerum, A. and Schreurs, G., 2023. Tectonic interactions during rift linkage:
1037 Insights from analog and numerical experiments. *EGU Solid Earth*, 14, 389–407.
- 1038 Scholz, C. A., Cohen, A. S., Johnson, T. C., King, J., Talbot, M. R., and Brown, E. T. (2011). Scientific
1039 drilling in the Great Rift Valley: The 2005 Lake Malawi Scientific Drilling Project—An overview of
1040 the past 145,000 years of climate variability in Southern Hemisphere East Africa. *Palaeogeography,*
1041 *Palaeoclimatology, Palaeoecology*, 303(1–4), 3–19.
- 1042 Scholz, C.A. and Rosendahl, B.R., 1988. Low lake stands in Lakes Malawi and Tanganyika, East Africa,
1043 delineated with multifold seismic data. *Science*, 240(4859), pp.1645-1648.
- 1044 Scholz, C.A., Shillington, D.J., Wright, L.J., Accardo, N., Gaherty, J.B., Chindandali, P. (2020). Intrarift
1045 fault fabric, segmentation, and basin evolution of the Lake Malawi (Nyasa) Rift, East Africa.
1046 *Geosphere* 16 (5), 1293–1311.
- 1047 Specht, T. D., and Rosendahl, B. R. (1989). Architecture of the Lake Malawi Rift, East Africa. *J. Afr.*
1048 *Earth Sci.* 8 (2–4), 355–382. doi:10.1016/s0899-5362(89). 80032-6.
- 1049 Stamps, D. S., Calais, E., Saria, E., Hartnady, C., Nocquet, J. M., Ebinger, C. J., & Fernandes, R. M.
1050 (2008). A kinematic model for the East African Rift. *Geophysical Research Letters*, 35, L05304.
1051 <https://doi.org/10.1029/2007GL032781>.
- 1052 Stamps, D.S., Saria, E., Kreemer, C. (2018). A geodetic strain rate model for the East African Rift
1053 system. *Sci. Rep.* 8 (1), 1–8.
- 1054 Stevens, V.L., Sloan, R.A., Chindandali, P.R., Wedmore, L.N., Salomon, G.W., Muir, R.A., 2021. The
1055 entire crust can be seismogenic: evidence from Southern Malawi. *Tectonics* 40(6).
1056 <https://doi.org/10.1029/2020TC006654>.
- 1057 Sun, M., Gao, S.S., Liu, K.H., Mickus, K., Fu, X. and Yu, Y., 2021. Receiver function investigation of
1058 crustal structure in the Malawi and Luangwa rift zones and adjacent areas. *Gondwana Research*, 89,
1059 pp.168-176.
- 1060 Thomas, R.J., Fullgraf, T., Macey, P.H., Boger, S.D., Hölttä, P., Lach, P., Le Roux, P., Dombola, K.
1061 and Zammit, C. (2022). The Mesoproterozoic Nampula Subdomain in southern Malawi: Completing
1062 the story from Mozambique. *Journal of African Earth Sciences*, 196, p.104667.
- 1063 Toda, S., R. S. Stein, K. Richards-Dinger and S. Bozkurt, 2005, Forecasting the evolution of seismicity
1064 in southern California: Animations built on earthquake stress transfer, *Journal of Geophysical*
1065 *Research*, v. 110, B05S16, doi:10.1029/2004JB003415.

- 1066 Wedmore, L.N., Williams, J.N., Biggs, J., Fagereng, Å., Mphepo, F., Dulanya, Z., Willoughby, J.,
1067 Mdala, H., Adams, B., 2020a. Structural inheritance and border fault reactivation during active early-
1068 stage rifting along the Thyolo fault, Malawi. *J. Struct. Geol.* 139, 104097.
- 1069 Wedmore, L.N.J., Biggs, J., Williams, J.N., Fagereng, Å., Dulanya, Z., Mphepo, F. and Mdala, H.,
1070 2020b. Active fault scarps in southern Malawi and their implications for the distribution of strain in
1071 incipient continental rifts. *Tectonics*, 39(3), p.e2019TC005834.
- 1072 Williams, J.N., Fagereng, Å., Wedmore, L.N., Biggs, J., Mphepo, F., Dulanya, Z., Mdala, H.,
1073 Blenkinsop, T. (2019). How do variably striking faults reactivate during rifting? Insights from southern
1074 Malawi. *Geochem. Geophys. Geosyst.* 20 (7), 3588–3607.
- 1075 Williams, J.N., Wedmore, L.N., Scholz, C.A., Kolawole, F., Wright, L.J., Shillington, D.J., Fagereng,
1076 Å., Biggs, J., Mdala, H., Dulanya, Z. and Mphepo, F., 2022. The Malawi active fault database: An
1077 onshore-offshore database for regional assessment of seismic hazard and tectonic evolution.
1078 *Geochemistry, Geophysics, Geosystems*, 23(5), p.e2022GC010425.
- 1079 Wilson, D.S., 1990. Kinematics of overlapping rift propagation with cyclic rift failure. *Earth and*
1080 *Planetary Science Letters*, 96(3-4), pp.384-392.
- 1081 Wolf, L., Huismans, R.S., Wolf, S.G., Rouby, D. and May, D.A., 2022. Evolution of rift architecture
1082 and fault linkage during continental rifting: Investigating the effects of tectonics and surface processes
1083 using lithosphere-scale 3D coupled numerical models. *Journal of Geophysical Research: Solid Earth*,
1084 p.e2022JB024687.
- 1085 Van Wijk, J.W. and Blackman, D.K., 2005. Dynamics of continental rift propagation: the end-member
1086 modes. *Earth and Planetary Science Letters*, 229(3-4), pp.247-258.
- 1087 Yuan, X. P., Braun, J., Guerit, L., Simon, B., Bovy, B., Rouby, D., et al. (2019). Linking continental
1088 erosion to marine sediment transport and deposition: A new implicit and O(N) method for inverse
1089 analysis. *Earth and Planetary Science Letters*, 524, 115728.
1090 <https://doi.org/10.1016/j.epsl.2019.115728>
- 1091 Yuan, X. P., Braun, J., Guerit, L., Rouby, D., & Cordonnier, G. (2019). A new efficient method to
1092 solve the stream power law model taking into account sediment deposition. *Journal of Geophysical*
1093 *Research: Earth Surface*, 124, 1346–1365. <https://doi.org/10.1029/2018JF004867>
- 1094 Zwaan, F., Chenin, P., Erratt, D., Manatschal, G. and Schreurs, G., 2022. Competition between 3D
1095 structural inheritance and kinematics during rifting: Insights from analogue models. *Basin research*,
1096 34(2), pp.824-854.
- 1097 Zwaan, F. and Schreurs, G., 2017. How oblique extension and structural inheritance influence rift
1098 segment interaction: Insights from 4D analog models. *Interpretation*, 5(1), pp.SD119-SD138.

1099 **Figures**

1100

1101

1102

1103

1104

1105

1106

1107

1108

1109

1110

1111

1112

1113

1114

1115

1116

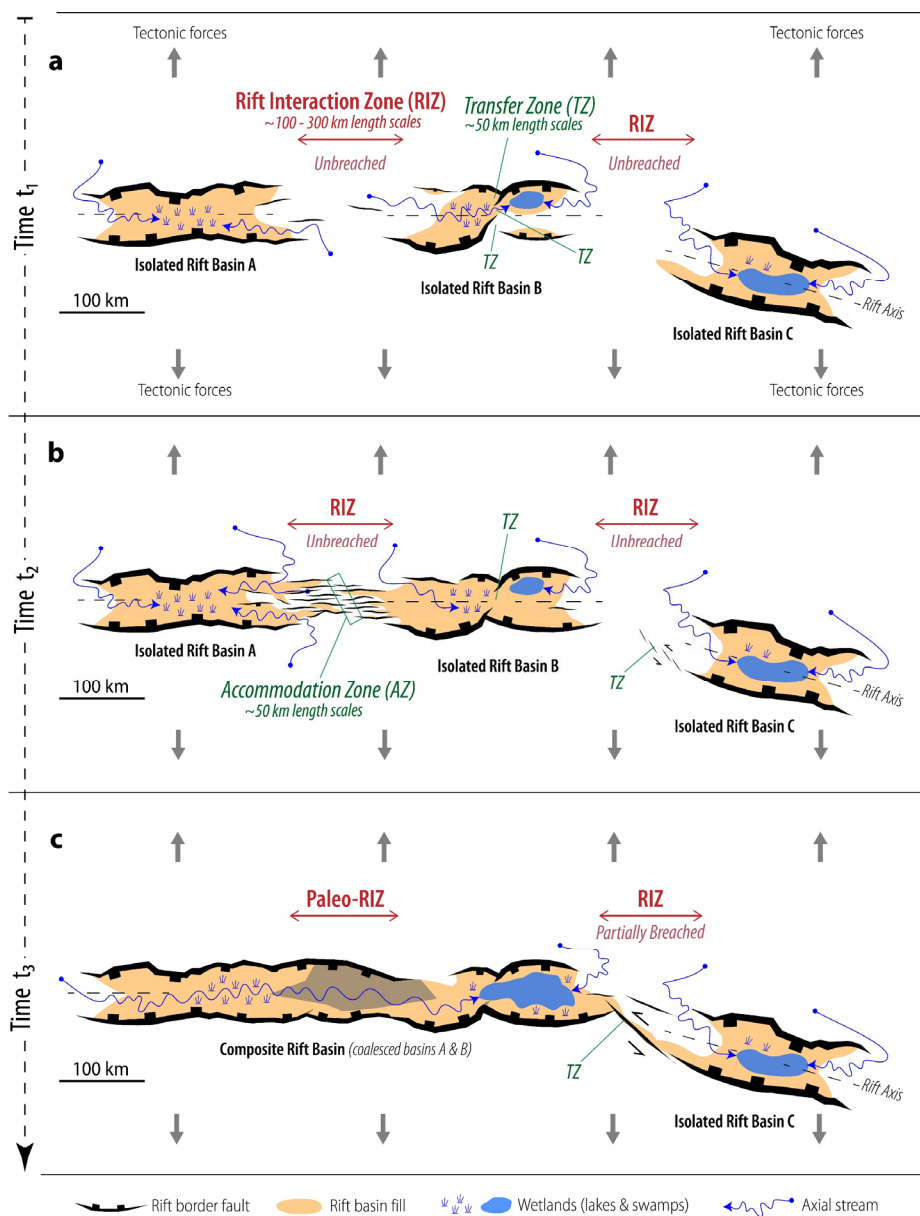
1117

1118

1119

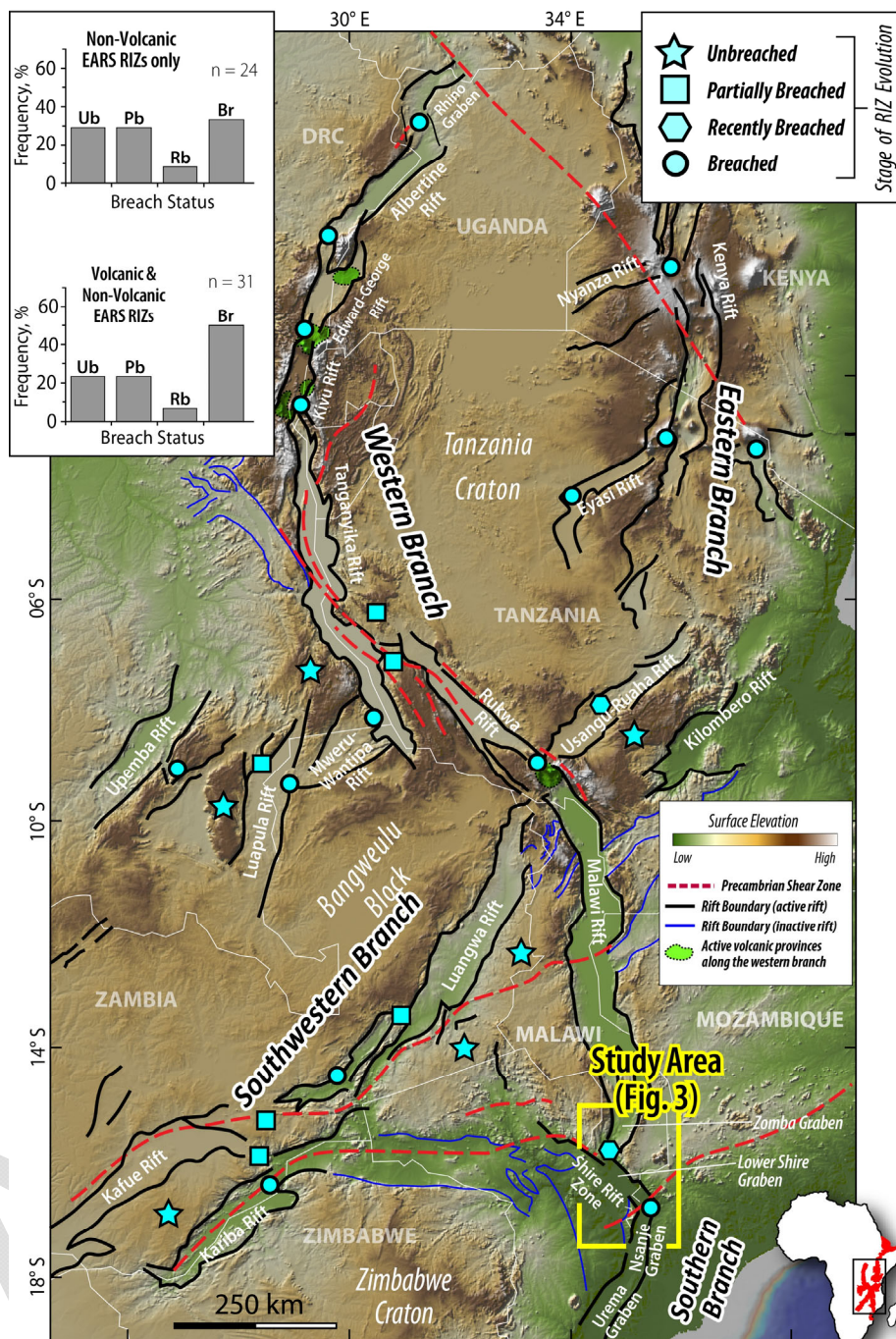
1120

1121

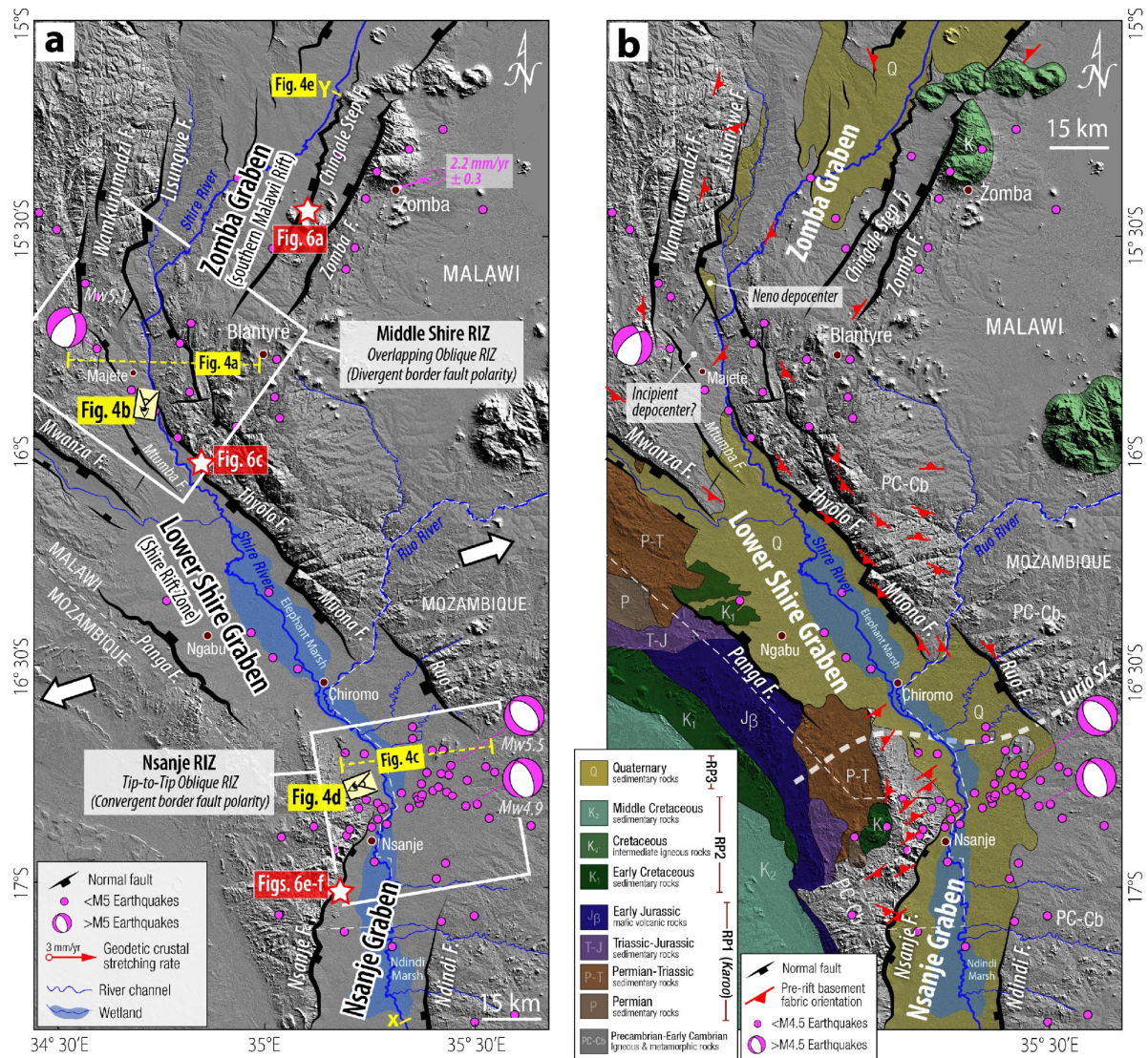


1122 **Figure 1.** Cartoon illustrating the evolution of zones of rift segment interaction along narrow continental rift
 1123 systems during (a) the initial nucleation of isolated rift basins, to (b) subsequent lateral propagation and
 1124 interaction, and (c) linkage and coalescence of the basins. Prior to linkage and coalescence, the broad region of
 1125 interaction between the rifts (~100 – 300-km length scales) are referred to as a ‘rift interaction zones (RIZ)’
 1126 (Nelson et al., 1992; Kolawole et al., 2021a). RIZs commonly host transfer and accommodation zones and their
 1127 associated structures that localize and transfer strain across the RIZs (Bosworth, 1985; Ebinger et al., 1987;
 1128 Morley et al., 1990; Nelson et al., 1992; Morley, 1995; Faulds and Varga, 1998). RIZ geometries can be defined
 1129 by the relative trend and border fault dip polarity of the interacting rift basins (after Morley et al., 1990) such
 1130 as Tip-to-Tip Collinear (e.g., between Rift Basins A and B in Panels a & b) and Underlapping oblique
 1131 convergent (e.g., between Rift Basins B and C in Panels a & b) (Kolawole et al., 2021a).

1132
1133
1134
1135
1136
1137
1138
1139
1140
1141
1142
1143
1144
1145
1146
1147
1148
1149
1150
1151
1152
1153
1154
1155



1156 **Figure 2.** Topographic relief map of the East African Rift System (EARS; Source: Ryan et al., 2009), showing
1157 the magma-rich eastern branch, and magma-poor western, southwestern, and southern branches. The symbols
1158 represent the stage of evolution of its rift interaction zones (RIZ), inferred from spatial extents of fault
1159 connectivity and topographic, and drainage morphology of the RIZs (Kolawole et al., 2021a). Histograms show
1160 the distribution of RIZ evolution stages along the rift system (from Kolawole et al., 2021a), and UB, PB, RP
1161 and Br are short for Unbreached, Partially breached, Recently breached, and breached respectively. Note that
1162 the EARS is defined by the active rift segments (black lines). *Bottom right inset:* Map of Africa showing the East
1163 African Rift System (red polygons) and region covered by the relief map (black rectangle).



1164

1165 **Figure 3. a.** Topographic relief map of southern Malawi and central Mozambique, showing the contiguous
 1166 Zomba Graben (Malawi Rift), the Lower Shire Graben (Shire Rift Zone), and Nsanje Graben, and their
 1167 intervening Middle Shire and Nsanje Rift Interaction Zones (RIZ). The main axial stream in the region, the
 1168 Shire River and its tributaries, drains all the three rift basins and flows further south into the Indian Ocean.
 1169 Fault segments are surface-breaking active faults from Williams et al. (2022) and Kolawole et al. (2022).
 1170 Earthquakes and focal mechanisms are from the US Geological Survey earthquake catalog, Global CMT
 1171 catalog, and Stevens et al. (2021) covering 1966 to 2020. Geodetic crustal stretching azimuth is from Stamps et
 1172 al. (2008, 2018). Basement metamorphic fabric orientations are from Williams et al. (2019), Kolawole et al.
 1173 (2022), Thomas et al. (2022), and field observations in this study. **b.** Geologic map of the southern Malawi
 1174 region and western Mozambique (modified after Choubert et al., 1988; Kolawole et al., 2022).

1175

1176

1177

1178

1179

1180

1181

1182

1183

1184

1185

1186

1187

1188

1189

1190

1191

1192

1193

1194

1195

1196

1197

1198

1199

1200

1201

1202

1203

1204

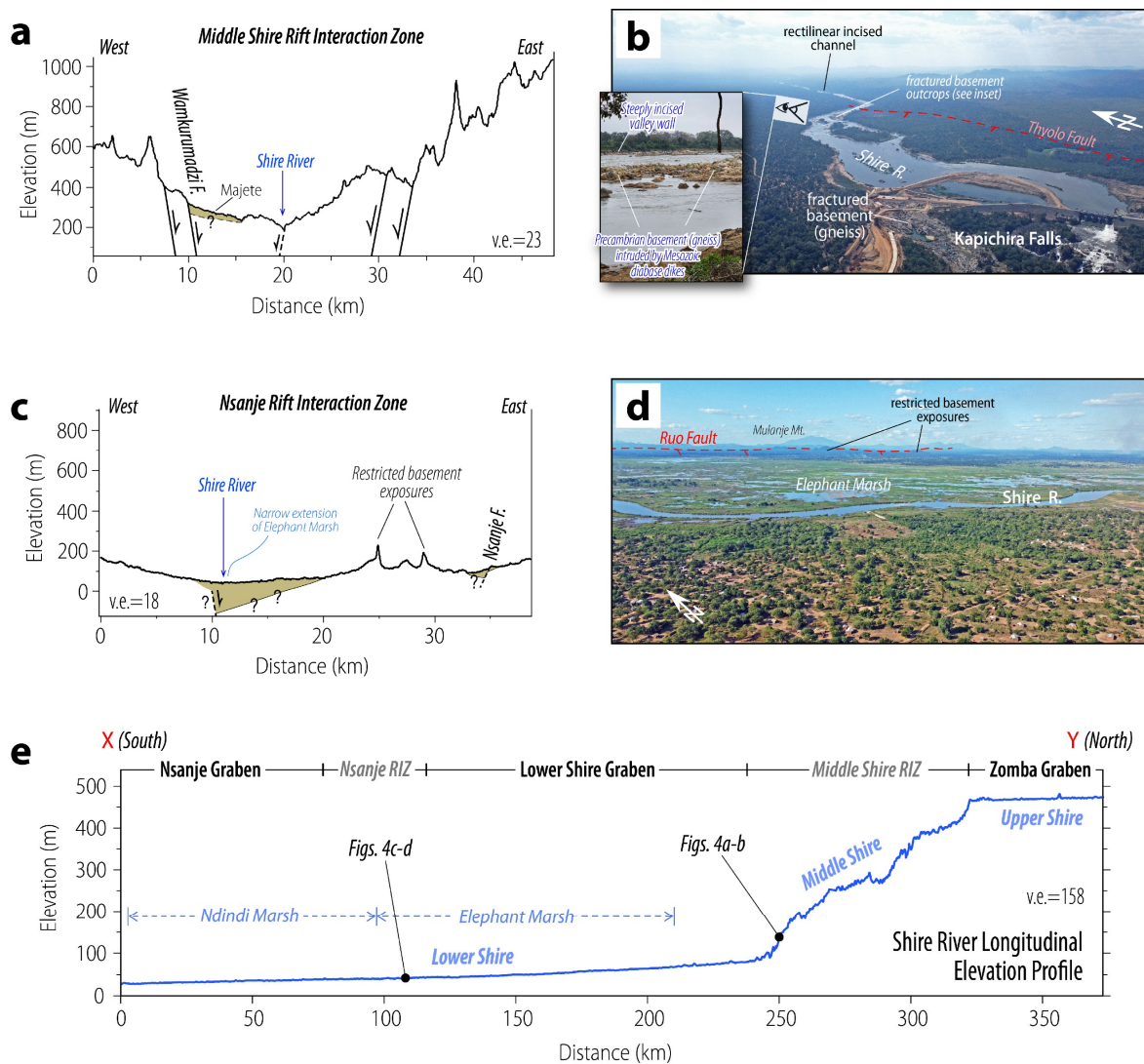


Figure 4. a – d. Topographic relief profiles (panels a & c; 30-m resolution Shuttle Radar Topography Mission data) and field photographs (panels b & d) showing rift morphology across the Middle Shire RIZ (a – b) and Nsanje RIZ (c – d). Sediment depocenters color coded in yellow. **e.** Longitudinal topographic relief profile of the Shire River (see Figure 3a for the start and end of the profile labelled as x and y).

1205
 1206
 1207
 1208
 1209
 1210
 1211
 1212
 1213
 1214
 1215
 1216
 1217
 1218
 1219
 1220
 1221
 1222
 1223
 1224
 1225
 1226
 1227
 1228
 1229
 1230
 1231
 1232
 1233
 1234

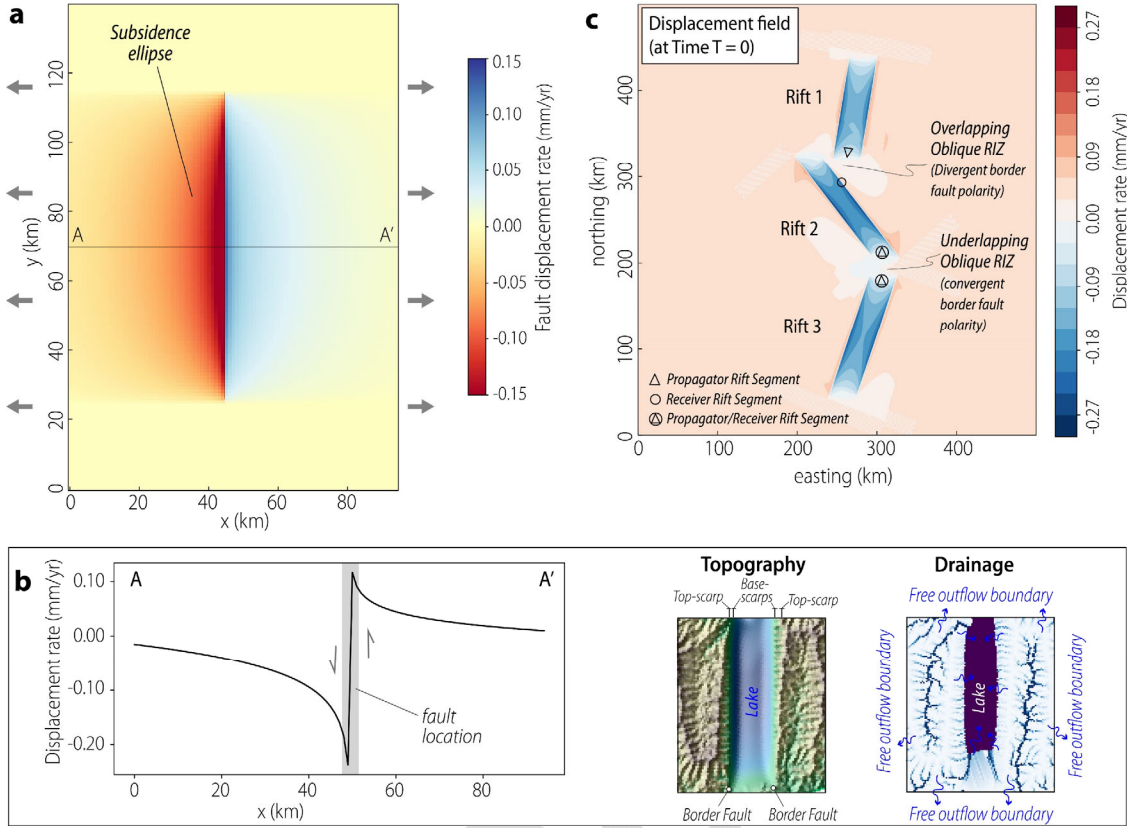
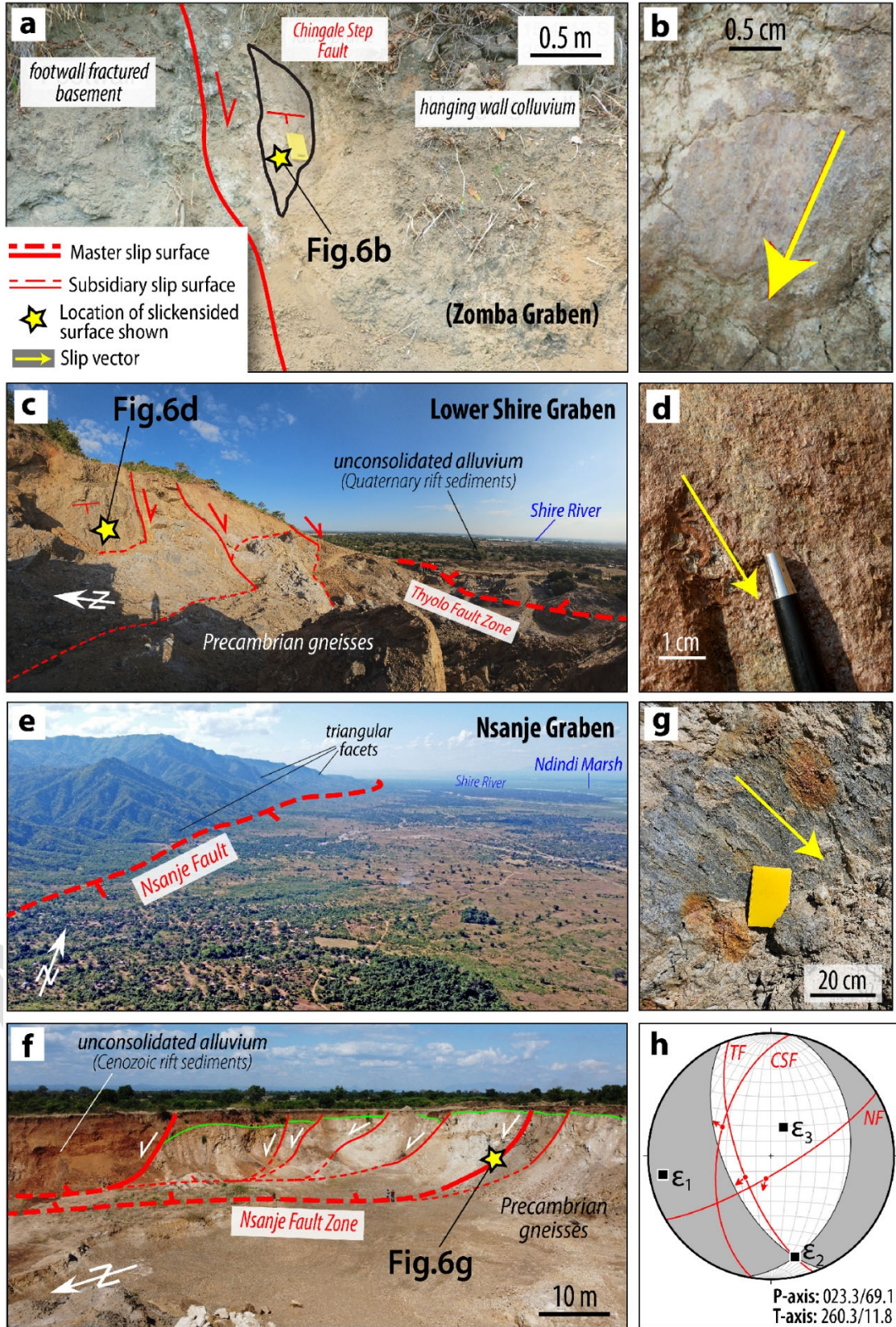


Figure 5. Model setup to simulate landscape evolution across two contiguous rift interaction zones with geometries similar to those of the Middle Shire and Nsanje rift interaction zones. **a - b.** Fault segment uplift field with hanging wall subsidence and footwall uplift. Inset maps in panel b shows the resulting topography and drainage for a graben configuration. **c.** Initial displacement field applied in the model to estimate the fault development and rift evolution.

1235
 1236
 1237
 1238
 1239
 1240
 1241
 1242
 1243
 1244
 1245
 1246
 1247
 1248
 1249
 1250
 1251
 1252
 1253
 1254
 1255
 1256
 1257
 1258
 1259
 1260
 1261
 1262



1263 **Figure 6. a – f.** Field photographs showing slip surfaces along the Chingale Step Fault, Zomba Graben (panels
1264 a – b; photographs from Wedmore et al., 2020b), Thyolo Fault, Lower Shire Graben (panels c – d), and the
1265 Nsanje Fault, Nsanje Graben (panels e – g). See Figure 3a for the location of the photos and look-direction of
1266 the landscape shots. **h.** Kinematic Tensor solution produced from the combined geological slip vectors
1267 measured along the three faults (i.e., Figures 7b, d, and g; see *Methods* section). ϵ_1 , ϵ_2 , and ϵ_3 represent the
1268 principal strain axes 1 (extension), 2 (intermediate), and 3 (shortening) respectively. The solution shows a
1269 predominantly normal faulting regime, although with a minor strike-slip component.

1270

1271

1272

1273

1274

1275

1276

1277

1278

1279

1280

1281

1282

1283

1284

1285

1286

1287

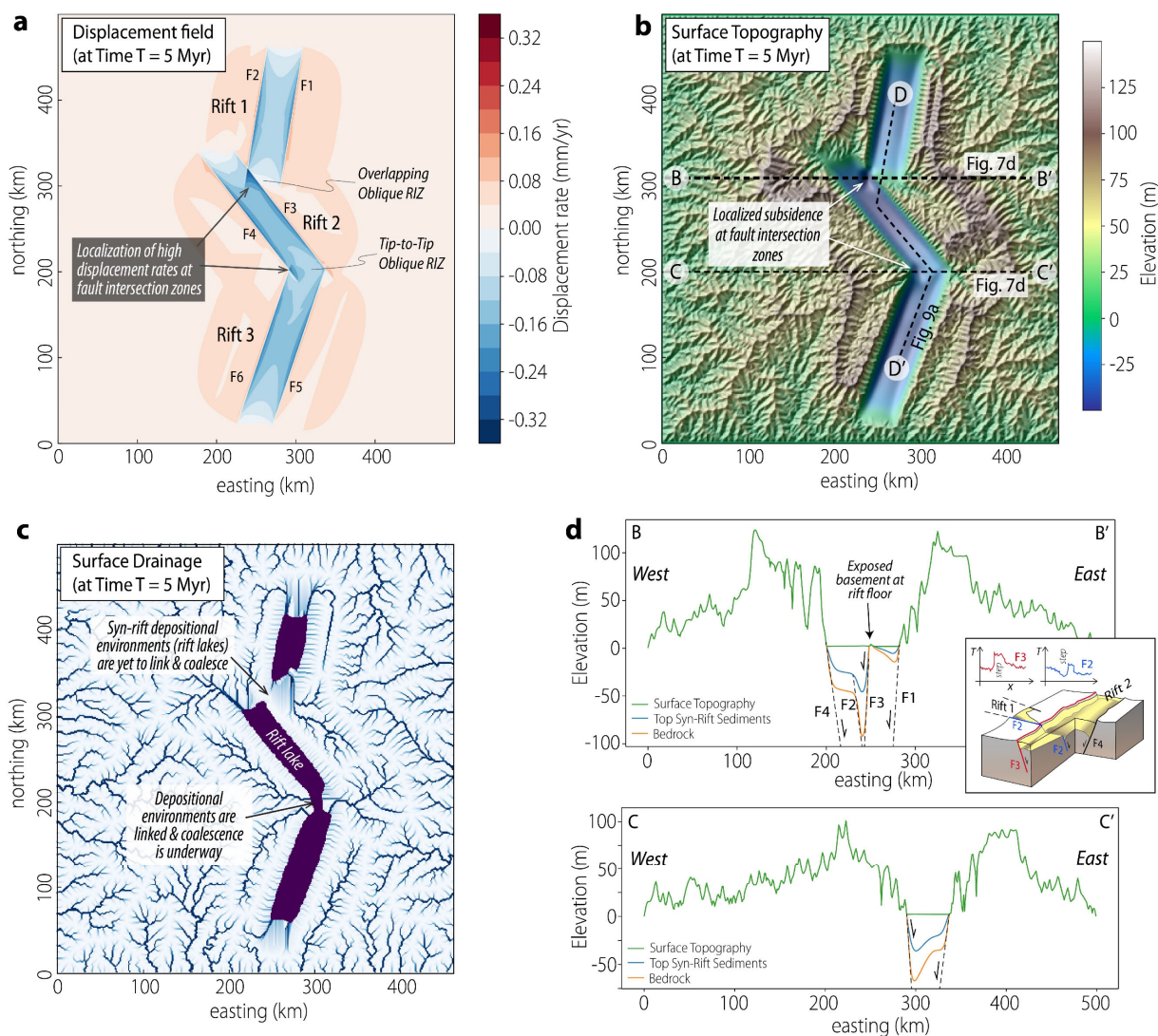
1288

1289

1290

1291

1292



1293
 1294 **Figure 7. a.** Displacement field, **b.** modeled topography, and **c.** drainage map at 5 Myr, showing the large-scale
 1295 fault structure and surface morphology of the laterally propagating and interacting rift tips. **d.** Cross-sections
 1296 A-A' across the overlapping oblique rift interaction zone (RIZ), and B-B' across the tip-to-tip oblique RIZ.
 1297 Note that the tip-to-tip oblique RIZ was initially an underlapping oblique RIZ at T=0 Myr (Figure 5c). *7d inset:*
 1298 3-dimensional (3D) schematic showing the large-scale structure of antithetically linked faults as seen in the
 1299 model results (Figs. 7a-b) and idealized throw-distance (T-x) plots inspired by the model results and natural
 1300 examples (e.g., Duffy et al., 2015).

1301
 1302
 1303
 1304
 1305

1306
 1307
 1308
 1309
 1310
 1311
 1312
 1313
 1314
 1315
 1316
 1317
 1318
 1319
 1320
 1321
 1322
 1323
 1324
 1325
 1326
 1327
 1328
 1329
 1330
 1331
 1332
 1333
 1334
 1335
 1336

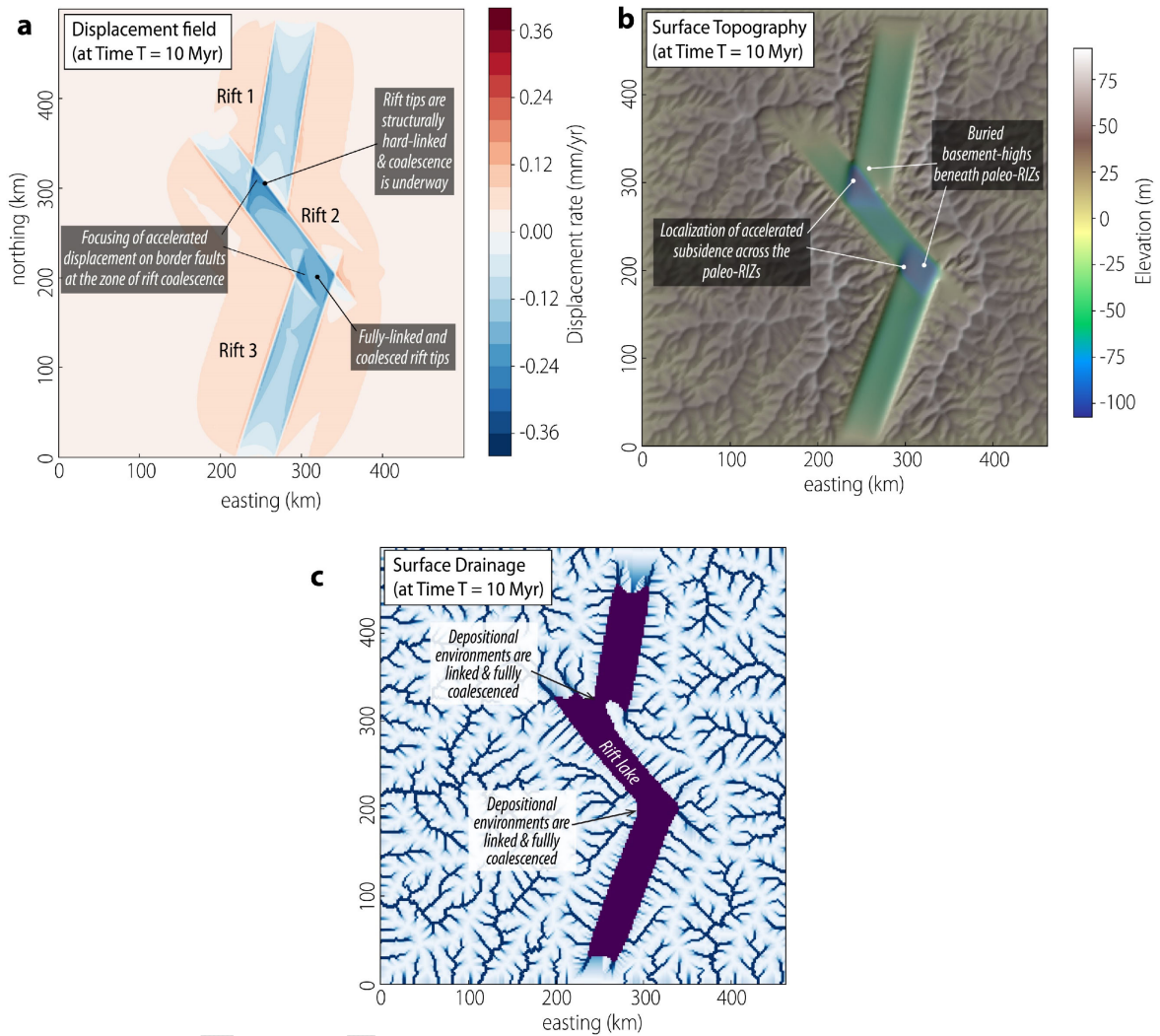
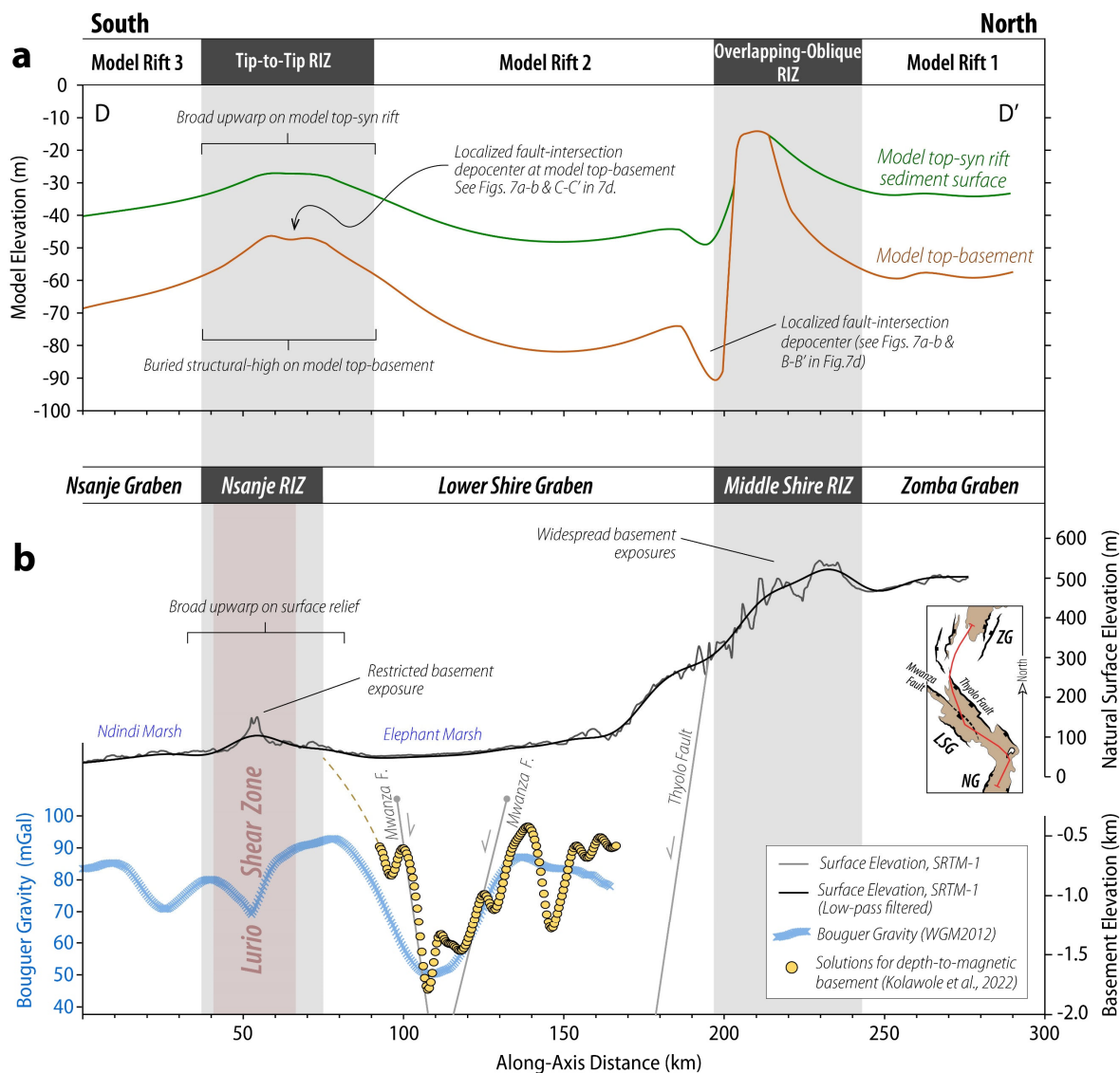


Figure 8. a. Displacement field, b. modeled topography, and c. drainage map at 10 Myr showing complete rift coalescence across the tip-to-tip RIZ and established hard-linkage with ongoing coalescence across the overlapping RIZ. Interestingly, the results also highlight that once rift linkage is established, rift coalescence is accompanied by the focusing of accelerated fault displacement and basin subsidence across the deforming RIZs.

1337

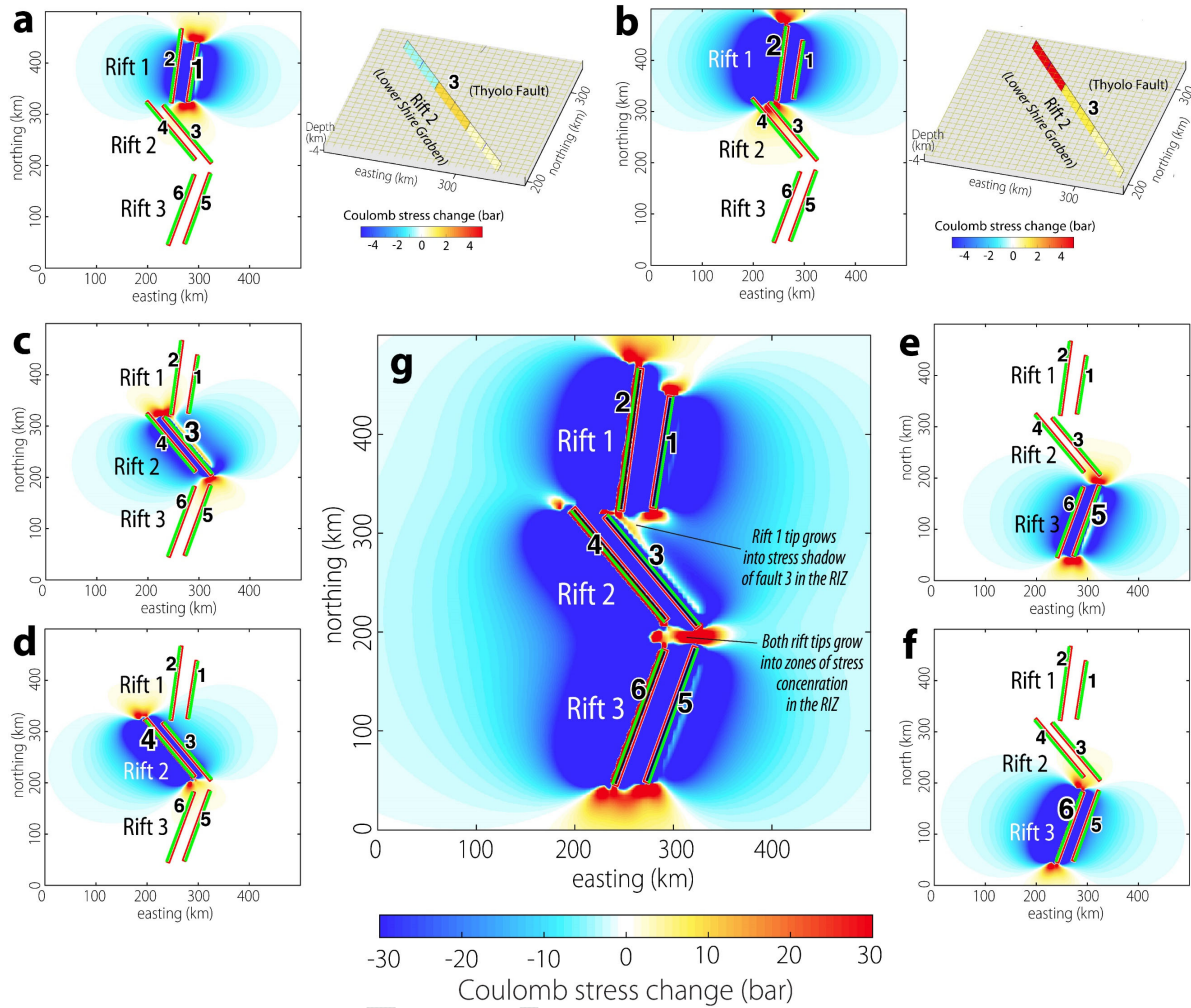


1338

1339 **Figure 9. a.** Plot comparing the along-axis model surface relief, model top-synrift surface relief, and model
 1340 top-basement relief (at 5 Myr time step) with the natural along-axis variation in surface topographic relief in the
 1341 studied rifts. See transect for profile D-D' in Figure 9b (modeled topography) and Figure S1 (natural
 1342 topography). **b.** Along-axis plot of natural surface relief along the rifts, Bouguer gravity anomaly, and variation
 1343 of basement elevation (transect in inset map; NG- Nsanje Graben, LSG- Lower Shire Graben, ZG- Zomba
 1344 Graben). The natural topography data is from 30 m-resolution Shuttle Radar Topography Mission (SRTM),
 1345 Bouguer gravity data from World Gravity global model, WGM2012 (Figure S3; Bonvalot et al., 2012), and
 1346 basement depths calculated from aeromagnetic grid (Kolawole et al., 2022).

1347

1348



1349

1350 **Figure 10. a – f.** Model results of predicted static Coulomb stress change distribution for instances of slip on
 1351 each of the border faults (as source fault, enlarged fault number) of the model rift basins, maintaining the same
 1352 input rift geometries and model parameters used for the Landscape evolution model. We assume a coefficient
 1353 of friction of 0.55, appropriate for the southern Malawi region (Williams et al., 2019), and fault rupture depth
 1354 of 5 km. In each model, the entire border fault length ruptures in a single event. Note that numbers 1 to 6
 1355 represent fault identifiers. 3-D views in panels a and b show Coulomb stress changes on fault 3 with slip on
 1356 source fault 1 (a) and fault 2 (b), illustrating the difference effects of these two fault slip events on the stress
 1357 field of fault 3 in the RIZ. **g.** Static Coulomb stress change distribution for the same model domain as shown
 1358 in a -f, but in which all the border faults act as source faults. Coulomb stress change is calculated for N-S
 1359 striking faults with a potential rake of -90 (normal dip-slip). Altogether, the models show that in overlapping
 1360 RIZs, the propagating rift tip grows into a stress relaxation zone, which contrasts tip-to-tip RIZs where
 1361 propagating rift tips grow into a compounding stress concentration zone.

1362